Selected topics in reaction studies with exotic nuclei

Nicolas Alamanos[1] and Alain Gillibert[1]

CEA/DSM/DAPNIA/SPhN Saclay,
91191 Gif-sur-Yvette Cedex, France

1 Introduction

The detailed study of unstable nuclei has been at the forefront of nuclear physics research for the last few years. With the continuous improvement in the intensities and optical qualities of secondary radioactive beams, mechanisms such as Coulomb excitation and more recently elastic and inelastic scattering, transfer and knock-out reactions are rapidly becoming standard tools for the investigation of the structure of nuclei far from stability. Here we are concerned essentially with the simplest of these processes, i.e. elastic and inelastic scattering, for which we will present recent experimental results and discuss briefly some theoretical developments aiming at obtaining nuclear structure information from them. We will also discuss recent measurements of transfer reactions and give an example of the role played by entrance channel potentials in the case of sub-barrier fusion involving weakly bound nuclei. Indeed, with the advent of radioactive beam facilities, interest in such studies with halo nuclei has renewed due to their specific features, like extended neutron densities, low-lying continuum, and very low energy breakup thresholds. It is expected that such features should appreciably affect fusion, as well as other reaction processes.

When moving away from the valley of stability, the ultimate goal of quasi-elastic reaction studies is to develop models and interaction potentials by uncovering novel manifestations of nuclear structure, such as new regions of deformation, the disappearance of shell closures or the appearance of new magic numbers.

2 Elastic scattering

Elastic scattering is the simplest reaction process. During the past few decades, electron, proton and neutron elastic scattering on stable targets has been a valuable tool for the investigation of nuclear properties. In the framework of a microscopic description, proton and neutron scattering is expected to provide information on the matter density (isoscalar density) near the surface of the nucleus. At high energies (E > 200 MeV) proton elastic scattering was also used to obtain information on the neutron density. As a matter of fact, from the combined analysis of electron and proton scattering, information on the neutron ground state density and transition density distribution can be obtained [1].

In these lectures we will present low energy elastic scattering results (E < 100 MeV) induced by light particles on unstable nuclei in inverse kinematics. A secondary beam of the radioactive nucleus of interest bombards a target containing light particles (p, d, t,..). The excitation energy and the scattering angle are deduced from the energy and angle of the recoiling light particle, detected with specially designed light particle detectors, like the MUST detector (see below).

2.1   Proton plus nucleus elastic scattering

When studying proton plus nucleus elastic scattering at energies well above the Coulomb barrier, it is adequate to ignore specific effects due to couplings to other reaction channels. It is then possible to describe the scattering by phenomenological or microscopic potentials that vary slowly with energy.

Summaries of many studies on stable nuclei have yielded optical model parametrizations such as that by F.D. Bechetti and G.W. Greenlees [2], which give good predictions for scattering cross sections. However, such approaches may encounter difficulties far from stability, due to the underlying assumption of similar interaction potentials for neutrons and protons. Moreover, the extracted parameters do not give direct access to the nuclear properties.

An alternative method is to use a microscopic approach. Microscopic optical model approaches have been used for many years to calculate the nucleon-nucleus and nucleus-nucleus entrance channel optical potential and transition potentials for scattering to excited states. We can divide the currently used microscopic approaches into two main categories:

α) In the first category, ground state and transition densities are used to deduce from infinite nuclear matter optical potential calculations the elastic scattering and the transition optical potentials of finite nuclei.

β) In the second category, ground state and transition densities are folded with an effective nucleon-nucleon interaction to generate ground state and transition potentials.

A very popular microscopic optical model description for obtaining the real and imaginary parts of the nucleon-nucleus optical potential is the JLM model developed by J.P. Jeukenne, A. Lejeune and C. Mahaux [3]. It belongs to the first category of microscopic calculations. The starting point for computing JLM potentials is the Brueckner-Hartree-Fock approximation and the Reid hard core nucleon-nucleon interaction which provide for energies up to 160 MeV the energy and density dependence of the isoscalar, isovector and Coulomb components of the complex optical model potential in infinite nuclear matter. For example, the real part of the optical model potential $V_0(\rho, E)$ is given by the expression:

$$V_0(\rho, E) = \sum \alpha_{ij} \rho^i E^{j-1}$$

where the coefficients α_{ij} are tabulated in [3].The spherical optical potential of a finite nucleus is obtained by applying the local density approximation. This approximation consists in replacing the infinite nuclear matter density by the density distribution of a finite nucleus. In that respect it provides root mean square radii which are too small. This was ascribed to the fact that it does not include accurately the effect of the range of the effective interaction. To improve this, the potential obtained in the local density approximation is convoluted with a Gaussian form factor $\sim \exp(-(r/t)^2)$ where t is the range parameter of the nuclear force. For more details see ref. [4].

The JLM central potential was extensively studied by Mellema et al. [5] and Petler et al. [6]. It is particularly successful in describing elastic proton scattering from stable nuclei, provided the imaginary potential is slightly re-adjusted by a normalization factor λ_w taking values usually between $0.8 < \lambda_w < 1.0$. For proton elastic scattering on light targets ($A < 40$), $\lambda_w \sim 0.8$ is particularly well suited. A value for the finite range parameter of $t = 1.0$ fm for both the real and the imaginary potentials has been found to yield better results than the initially used value of $t = 1.2$ fm.

In the case of elastic scattering, the nuclear ground state proton and neutron densities are required as input. For stable nuclei, the proton point-nucleon density ρ_p is obtained by unfolding the proton charge distribution from the charge density measured by electron scattering. The neutron density ρ_n is assumed to be the same as ρ_p for N=Z nuclei and in other cases is determined by assuming that $\rho_n = (N/Z)\rho_p$. For unstable nuclei proton and neutron densities are obtained by microscopic calculations.

Some typical JLM calculations are presented in Fig. 1, where proton elastic scattering on ^{16}O for different proton energies is compared to JLM theoretical predictions obtained with $\lambda_v = 1.0$ and $\lambda_w = 0.8$ [7]. The JLM optical potentials were computed using ^{16}O ground state densities obtained from electron scattering experiments [8]. As can be seen in Fig. 2, an equally good description is obtained of p+^{7}Li elastic scattering [7].

We have extended these calculations to unstable nuclei. In Fig. 3 proton elastic scattering angular distributions for ^{32}S, ^{38}S and ^{40}S measured respectively by D. Leo et al. [9] at $E_{lab} = 29.64$ MeV/nucleon, by J.H. Kelly et al. [10] at 39.0 MeV/nucleon and by F. Maréchal et al. [11] at 40.0 MeV/nucleon are presented together with JLM model calculations. New measurements on Sulphur elastic and inelastic scattering were recently obtained by E. Khan et al. [12] at $E_{lab} = 53.0$ MeV/nucleon. These new results will not be discussed in this paper. The proton and neutron ground-state densities were obtained from shell model calculations by A. Brown [13]. The imaginary part of the central optical potential was varied smoothly down to $\lambda_w \sim 0.8$ to better reproduce the experimental cross sections shown in Fig. 3. The full line corresponds to calculations with $\lambda_w = 0.8$ and the dotted line to calculations with $\lambda_w = 1.0$. Rather good agreement is obtained between the theoretical predictions and the data for $\lambda_v = 1.0$ and $\lambda_w = 0.8$. These calculations show the capability of the JLM model to reproduce elastic scattering angular distributions for unstable nuclei with values
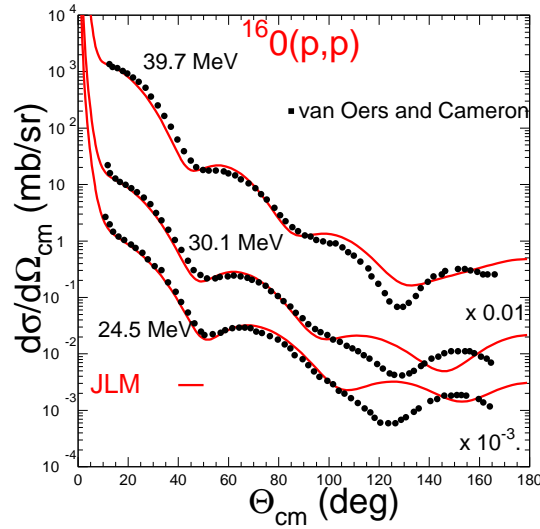
Fig. 1. Comparison between experimental data for proton elastic scattering on ^{16}O and JLM calculations with λ_v =1.0 and λ_w =0.8. The data are from ref. [6]

of λ_v and λ_w close to those obtained from elastic scattering studies involving stable nuclei.

Special attention has to be paid in the case of elastic scattering involving weakly bound nuclei. Here, couplings to the continuum are expected to play a significant role since the scattering states are much closer to the continuum states than in strongly bound nuclei. Indeed, these nuclei can be easily excited to unbound states or dissociate in the field of the target nucleus. ^6He, for instance, breaks up easily into an α particle and two neutrons. It was shown by V. Lapoux et al. [7] (see also Fig. 4) that ^{6}He+p and ^{8}He+p elastic scattering angular distributions, measured over a broad range of incident energies, are better reproduced by reducing significantly ($\sim$ 20%) the real part of the optical potential. A similar reduction of the real potential was observed a long time ago by G.R. Satchler and W.G. Love [14] in their systematic study of nucleus-nucleus elastic scattering with double-folded real potentials using the M3Y effective interaction. In the case of elastic scattering involving weakly bound ^{6}Li and ^{9}Be nuclei, they found that the double-folded potential had to be reduced by $\sim$ 40%. This reduction may be ascribed to the effect of couplings to unbound states (see below).

Recently E. Bauge et al. [15] extended the JLM calculations to higher energies. The original JLM model was re-investigated and several local density ap-
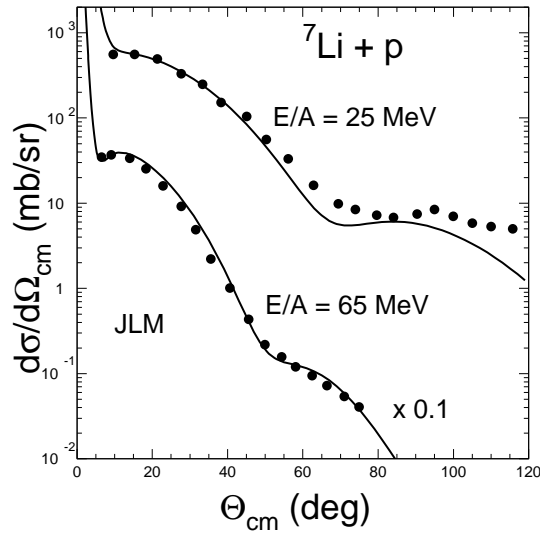
Fig. 2. Cross sections for ^{7}Li+p elastic scattering compared to calculations using the JLM potential from V. Lapoux et al. [7]

proximations (LDA) and spin-orbit prescriptions were examined to select those which provide the best overall description of elastic scattering and reaction measurements. Over three hundred data sets, for stable nuclei with ($A > 40$), including differential cross sections, analysing powers, spin rotation functions, and reaction cross sections have been compared to the theoretical calculations. A good overall description of the scattering and reaction measurements available up to 200 MeV was obtained. A comparison of the theoretical predictions with ^{30,38,40}S(p,p) elastic scattering data is presented in Fig. 5. The same authors [11] have extended the Bruyères-JLM model to treat inelastic scattering of deformed nuclei.

What is remarkable with the different JLM-type calculations, is that for all of them, with the exception of scattering involving weakly bound nuclei, the normalization factor λ_v of the real potential for proton scattering in the energy region between 10 and 80 MeV, is close to one. The normalization factor of the imaginary potential λ_w is also rather constant, and close to 0.8 for nuclei with mass ($A < 40$) or close to 1.0 for ($A > 40$). In the Bruyères-JLM model and for nuclei with $A > 40$, the λ_w is also constant and close to 1.2. The main origin of this difference is probably that in the Bruyères-JLM model the imaginary part of the effective interaction is multiplied by an effective mass [15].
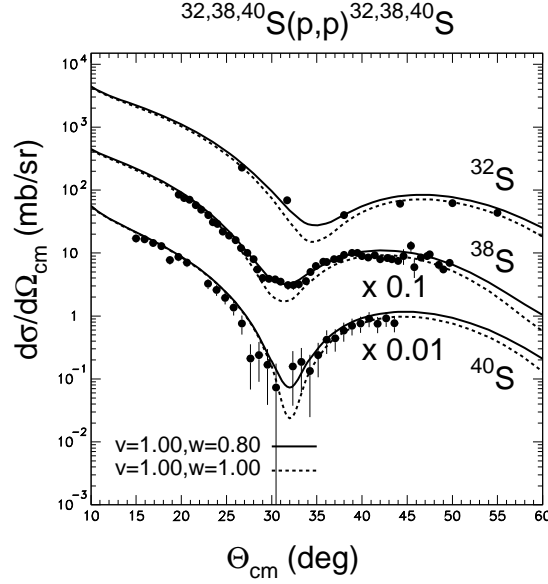
^{32,38,40}S(p,p)^{32,38,40}S

Fig. 3. From top the bottom elastic scattering of ^{32}S, ^{38}S and ^{40}S respectively on proton targets. The curves correspond to JLM model theoretical calculations from N. Alamanos et al. [13]

The rather constant values of λ_v and λ_w which are necessary in JLM-type calculations to describe successfully proton elastic scattering in a broad mass and energy domain allow us to consider that these calculations have some predictive power.

In the second category of microscopic models used to reproduce proton plus nucleus direct reaction data belong models in which a realistic density dependent nucleon-nucleon interaction is used as effective interaction. The basic inputs are the nuclear densities of the nucleus and an effective nucleon-nucleon (NN) interaction. Dao T. Khoa et al. [16], proposed recently a folding model for the analysis of proton plus nucleus elastic and inelastic scattering. The long experience of this group, gained in successful folding model analyses of nucleus-nucleus elastic scattering data, helped in choosing the most appropriate (NN) interaction [17]. This approach provides the central part of the local, real, energy dependent, proton-nucleus potential. However, since the nucleon-nucleon interaction used in this formalism is real, it provides only the real parts of the elastic and inelastic nucleon-nucleus potentials. For the imaginary potential, a standard Woods-Saxon (WS) form is used. Elastic and inelastic cross sections for proton scattering on ^{38}S are presented in Fig. 20. The calculations give a rather good account of the data. More details concerning these calculations are
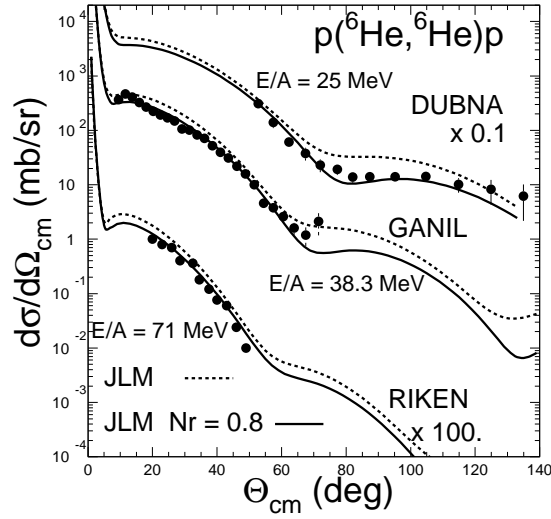
Fig. 4. The ^{6}He data obtained at GANIL at 38.8 MeV/nucleon are plotted with data obtained at Dubna at 25 MeV/nucleon and at Riken at 71 MeV/nucleon. The lines are JLM calculations with $\lambda_v =1.0$ dashed lines and $\lambda_v =0.8$ solid lines.

presented in chapter 3. This approach was applied to study elastic and inelastic proton scattering on $^{30-40}$S, as well.

A comparison between the predictions of the currently used microscopic models of the properties of the first 2^+ excited states of the S isotopes will be presented in the chapter describing inelastic scattering.

K. Amos et al.[18] have developed a more sophisticated and ambitious version of the single-folding formalism presented above. In their approach one calculates the complex non-local nucleon-nucleus potential without localization of the exchange amplitudes using the explicit expression for each single-particle wave function taken, e.g. from the shell model. The potential is obtained in coordinate space by folding a complex energy- and density-dependent effective (NN) interaction with the one-body density-matrix elements (OBDME) and single particle bound states of the target generated by shell model calculations. As the approach accounts for the exchange terms in the scattering process, the resulting complex optical potential is non-local. This model has been applied successfully to calculate elastic and inelastic scattering of protons from many stable and unstable nuclei. The structure of the weakly bound nuclei ^{6,8}He and ^{9,11}Li was also studied and a halo structure was confirmed for ^{11}Li with a non-halo one
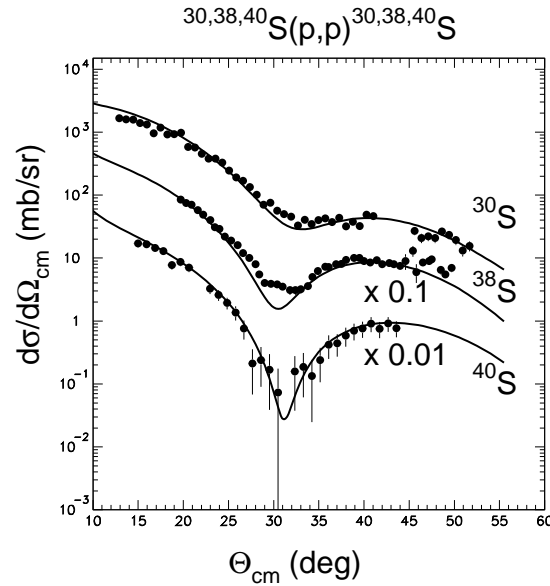
Fig. 5. Elastic scattering data of ^{30}S, ^{38}S and ^{40}S on proton targets are presented from top to bottom respectively. The ^{30}S elastic scattering data were obtained from [12]. The curves correspond to Bruyères-JLM model theoretical calculations.

for both ^{8}He and ^{9}Li [19]. The available elastic scattering data for ^{6}He are not extensive enough to discriminate between halo and non-halo structure. This can be observed in Fig. 22 where p+ ^{6}He data are compared to halo (solid line) and no halo (dashed line) calculations.

Furthermore, this formalism was successfully used for calculating reaction cross sections for nucleon-nucleus scattering up to 300 MeV [20].

2.2   The MUST detector

The silicon strip Nowadays, the study of exotic nuclei is generally performed with radioactive beams. In the case of quasi-elastic reactions on light targets this usually means inverse kinematics, which implies a forward focusing for the scattered heavy projectile. The detection of the projectile is not the best way to characterize the reaction, for several reasons: i) it is difficult to measure unbound states due to particle emission, ii) even for bound states (except the ground state), the levels are broad due to in-flight photon emission, iii) this focusing may be so strong that the experimental resolution is no longer good enough to extract the scattered particle angular distributions for each individual level.

An alternative solution consists in the detection of the recoil target nuclei, which is exactly equivalent to the detection of the scattered ejectiles in the case

of two-body reactions. For example, in the case of the elastic scattering [10]C (p,p) [10]C of Fig. 6, this corresponds to the detection of the recoiling proton rather than the [10]C ejectile. The recoil nuclei have generally much lower energies than the ejectile, so that energy loss in the target will be a problem. Therefore, this method is most suitable for thin targets with low atomic numbers, like polypropylene CH_2 or CD_2 foils. The main issues will be elastic and inelastic scattering on proton or deuteron targets, as well as transfer reaction. The kinematics of elastic and inelastic scattering of [10]C projectiles (left) on a proton target and the kinematics of one neutron transfer (p,d) reactions (right), studied in [21] and [22] are illustrated in Fig. 6 with the kinematical loci of the ground state and fictive states at excitation energies of 1 and 2 MeV.
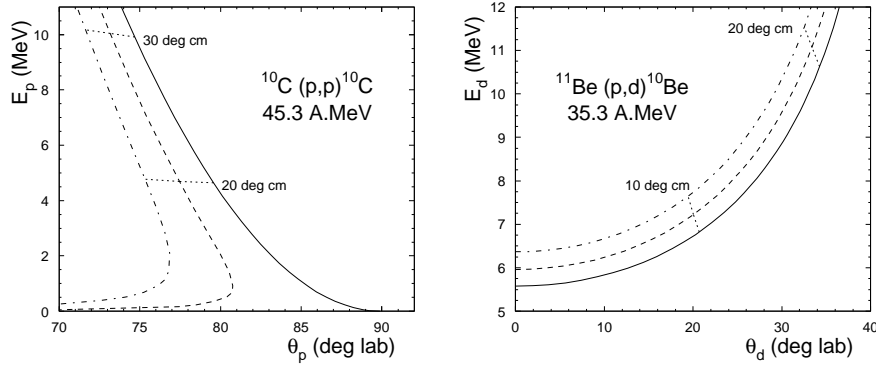

Fig. 6. Elastic and inelastic scattering of [10]C projectiles (left) and one neutron transfer (right) on a proton target. The energy and angle of the recoil nuclei, respectively proton and deuteron, are shown for the ground state (full line) and two fictive states at 1MeV and 2 MeV (dashed and dot-dashed lines)

With the recoil nucleus method, there is no limitation on the measurement of unbound states of the projectile at excitation energies larger than the particle emission thresholds.

The MUST array is composed of 8 independent modules, each of them being composed of three detectors (Si-strip, Si-Li, CsI) with their own electronics and cooling. The most original part of the MUST device consists in the first stage [23], which is a 300 μm thick, 60x60 mm^2 double sided Si-strip detector with 60 horizontal and 60 vertical strips. Low energy particles like those detected in elastic scattering at small cm angles are stopped in that stage. They are identified in a scatter plot (Fig. 7) by their energy and time of flight, which requires an external beam correlated time signal. The identification does not only depend on

the distance between the detector and the target, but also on the time resolution of the external signal. As the optical qualities of the secondary beams are not good enough, the RF signal of Fig. 7 is replaced by the time signal of additional beam tracking detectors [24]. These detectors also allow the reconstruction of the trajectory of the beam on the target with a position resolution equal to 1mm and an angular resolution of 0.5 degree. This step is the determining factor in improving the global excitation energy resolution.
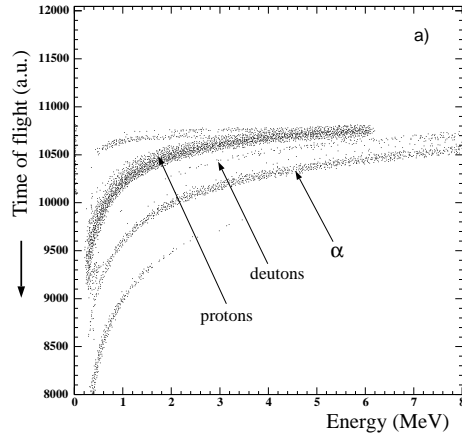

Fig. 7. Scatterplot of energy measured in the Si-strip detector versus the time of flight between the strip detector and the cyclotron RF signal. Protons with energy below 6 MeV are stopped in the strip detector and go through for energies above.

The recoil angle with respect to the beam direction is determined from the strips.

Higher energy particles are stopped and identified (using the ΔE - E method) with the following detectors, a 3mm thick Si-Li detector and a 3cm thick CsI crystal. In the case of protons, the maximum energy for which the protons are stopped in each stage is 6 MeV (Si-strip detector), 24 MeV (Si-Li detector) and 103 MeV (CsI scintillator).

An important parameter is the excitation energy resolution. It results from many effects, depending on the particle energy and the reaction considered. The target thickness plays an important role due to the fact that both the reaction vertex inside the target and the angular straggling for very low energy particles are unknown. A typical result is shown in Fig. 8 for elastic scattering of ^{11}C on a 1.5 mg/cm^2 thick CH_2 target, with an energy resolution (FWHM) $\delta E^* = 700$ keV.
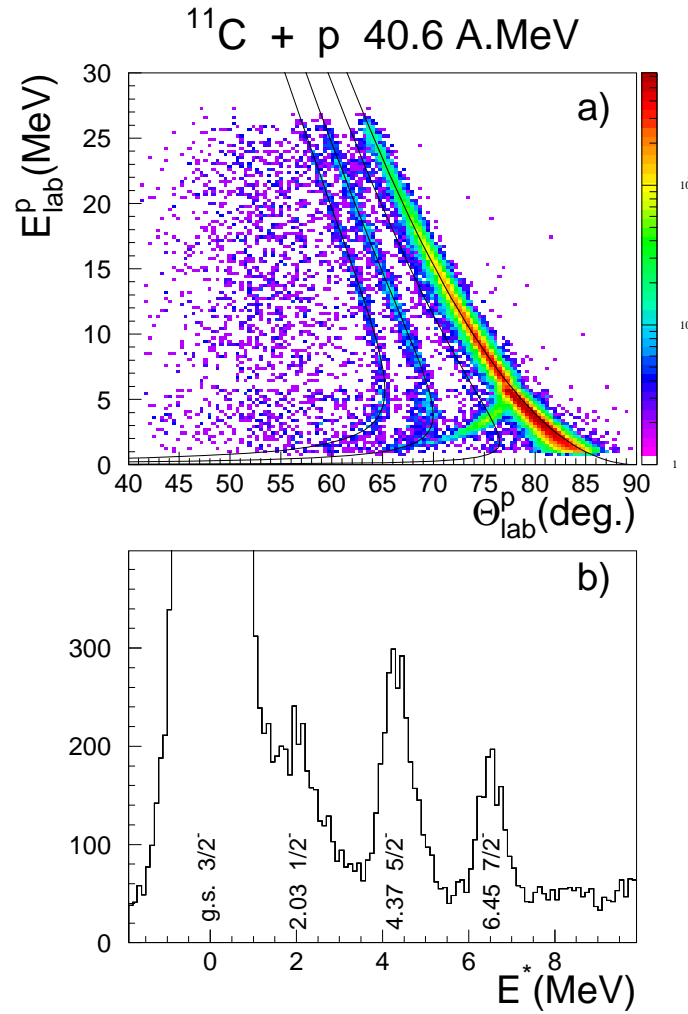
Fig. 8. Experimental elastic scattering of ^{11}C + p at 40.6 A.MeV : the upper part is identical to Fig. 6 (left) with kinematical lines superimposed on data; the lower part is obtained after calculation of the excitation energy event by event, with evidence for the excitation of states in ^{11}C at 2.03, 4.37 and 6.45 MeV. The excitation energy resolution is 700 KeV.

2.3 Weakly bound nucleus-nucleus elastic scattering

During the last few decades, the double folding model has been widely used by many groups to describe heavy ion scattering. In this model the potential is obtained by folding the ground state density distributions of the two interacting nuclei with an effective (NN) interaction [14]:

$$U_F(\boldsymbol{R}) = \int d\boldsymbol{r}_1 \int d\boldsymbol{r}_2 \rho_1(\boldsymbol{r}_1) \rho_2(\boldsymbol{r}_2) v(\boldsymbol{r}_{12})$$

where $\boldsymbol{R}$ is the radius vector connecting the centres of mass of the projectile and target nuclei, $\boldsymbol{r}_i$ are the radius vectors from the centre of mass of nucleus i to each of its constituent nucleons, $\boldsymbol{r}_{12} = \boldsymbol{r} + \boldsymbol{r}_2 - \boldsymbol{r}_1$ and $v(\boldsymbol{r}_{12})$ is the effective (NN) interaction. The original version of the folding model based on the M3Y effective (NN) interaction, introduced by G.R. Satchler and W.G. Love, seems to deliver satisfying results in most cases where the heavy ion interaction is dominated by strong absorption, i.e. when elastic scattering data are sensitive to the heavy ion optical potential only in the surface region. Success for the folding model is considered if an overall good description of the experimental data is obtained with a normalization coefficient N_R of the optical potential close to unity. It is also well established that when the data are sensitive to the optical potential over a wider radial domain, the simple double folding model fails to give a good description of the experimental results. A first attempt to take into account explicitly the density dependence of the M3Y interaction was presented in ref. [25]. Recently this approach was generalized for the calculation of the nucleus-nucleus potential using new versions of the density dependent M3Y interaction (BDM3Y1, CDM3Y6,...) which reproduce consistently the saturation binding energy and density of normal nuclear matter [26]. These new versions of the M3Y interaction describe successfully heavy ion elastic scattering data that are sensitive to the real potential not only at the surface but also at smaller distances.

On the reduction of the nucleus-nucleus optical potential

It is also well established that folding model analyses of elastic scattering involving weakly bound nuclei i.e. ^{6}Li, ^{9}Be, at incident energies lower than 150 MeV, with the old non density dependent M3Y interaction or the new density dependent versions of the M3Y interaction, require a reduction of the real part of the optical potential N_R by about $\sim 40\%$ [14],[27]. In their pioneer work on the description of elastic scattering using the double folding model, G.R. Satchler and W.G. Love pointed out the failure of their calculations to describe ^{6}Li and ^{9}Be scattering data and made a premonitory statement that ...*The only exception established so far occurs for the scattering of* ^6Li *and* ^9Be *which require a reduction of the calculated potential by a factor* N_R *of two. The reason for this is not known at present, but presumably it is associated with the weak binding energy of these nuclei....*

Several authors have shown the need to reduce the folding model optical potential in order to describe ^{6}Li and ^{9}Be elastic scattering data on different

targets. This reduction of the potential was recently confirmed by Trache et al. [28] for the description of several weakly bound light elements, leading to renormalization factors of $N_R \sim 0.66$ to 0.37 depending on the interaction used. It has to be noted that the mean normalization factor was $N_R \sim 0.6$ for a BDM3Y1 interaction [29]. Furthermore, A. Pakou et al. [30] have systematically analysed in the same folding framework, simultaneously with new ^{6}Li+^{28}Si elastic scattering data at near barrier energies, previous data of ^{6}Li on various targets and energies. The real part of the entrance channel optical potential was calculated within the double folding model by using the BDM3Y1 interaction. The imaginary potential was assumed to be the same folded potential, but with a different normalization factor N_I. The results concerning the real and imaginary parts of the potentials are presented in Fig. 9. They are consistent with optical potentials where the normalization factor N_R for energies both near and above the Coulomb barrier are almost independent of energy and target and close to $N_R \sim 0.6$. We would like to note here that the behaviour of the real and imaginary parts of the potentials for energies around the Coulomb barrier does not show the so-called sub-threshold anomaly. However, this discussion goes beyond the scope of the present paper, see [30], [31] and references therein.
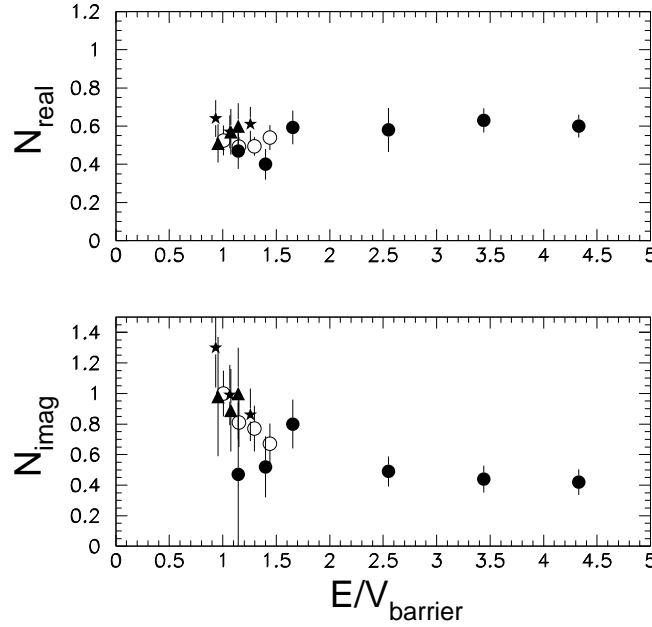

Fig. 9. Normalization factors of the real and imaginary potentials as a function of the ratio of the ^{6}Li bombarding energy over the Coulomb barrier. Solid circles correspond to data for the ^{6}Li+^{28}Si system, open circles to the ^{6}Li+^{58}Ni, triangles to the ^{6}Li+^{118}Sn system and stars to the ^{6}Li+^{208}Pb system.

The polarization potential

By a complete coupled channels reaction model Sakuragi has shown that the reduction of the real potential, which is necessary to describe elastic scattering data with ^{6}Li and ^{9}Be projectiles, is due to strong couplings of the break-up channels to the elastic channel of these loosely bound nuclei [32]. We can therefore anticipate that scattering of weakly bound nuclei can be described either by complete coupled channel calculations, namely by continuum discretized coupled channel calculations (CDCC) or by reducing the real part of the folded potential. The origin of this reduction is the presence of a repulsive polarization potential.

The elastic scattering of two heavy ions can be strongly influenced by coupling to non-elastic channels. Formally, this can be taken into account by introducing a polarization potential, in addition to the original bare potential, in the elastic scattering Schrödinger equation:

$$U = V_{bare} + \Delta U,$$

where $\Delta U = \Delta V + i\Delta W$ is the polarization potential. The bare potential can be phenomenological or it can be obtained from folding model calculations. The break-up effect can be represented by a dynamical polarization potential which has a strongly repulsive real part in the surface and an additional absorptive (imaginary) part [32]. There have been several studies of polarization potentials and analytical expressions were obtained, particularly for pure Coulomb excitation [33], [34], where the problem is essentially solved. For nuclear inelastic excitation and transfer, an analytical expression for the imaginary part of the polarization potential was obtained using a semi classical approach by Pollarolo et al. [35]. Furthermore, Z. El-Itaoui et al. [36] using the plane-wave approximation derived analytical expressions for both the real and the imaginary parts of the polarization potential arising from nuclear inelastic excitations. However, a more general approach for obtaining the real and the imaginary parts of the polarization potential in the presence of couplings to states in the continuum, which is the usual situation in scattering involving weakly bound nuclei, is still missing.

Dao T. Khoa et al., [27], in a systematic study of the energy dependence of ^{6}Li+^{12}C elastic scattering, using a bare potential obtained from their folding model calculations with a BDM3Y1 effective interaction, found that the polarization potential becomes weaker at incident energies higher than 150 MeV. More importantly, they showed that for scattering results which are sensitive to the nuclear potential not only at the surface of the colliding nuclei but also at smaller distances, a renormalization of the folded potential as a whole is not a correct approach [26]. V. Lapoux et al. [37] reached similar conclusions using a bare potential obtained from folding model calculations using the CDM3Y6 effective interaction. New extended data for elastic scattering of ^{6}He on ^{12}C, without any contamination from target excitations, were reported by V. Lapoux et al. [37]. In the analysis of the data a complex surface potential with a repulsive real part was added to the bare potential, which was generated by folding model calcula-
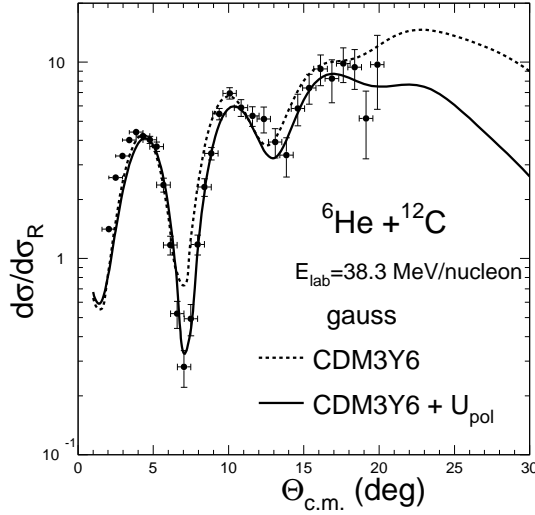
Fig. 10. Elastic scattering for ^{6}He+^{12}C at 38.3 MeV/nucleon. The optical model calculations were obtained with folding model optical potentials generated with Gaussian shape density distributions for ^{6}He.

tions using the CDM3Y6 effective interaction. The role of the surface potential is to simulate the surface effects induced by the polarization potential. In the optical model calculations, a Woods Saxon imaginary potential with the same depth and radius as found in the ^{6}Li+^{12}C case was used. The optical model calculations are compared to the data in Fig. 10 and Fig. 11.

The dashed curve in Fig. 10 is obtained by using a CDM3Y6 optical potential generated with a Gaussian shape density distribution for ^{6}He. The solid curve is obtained by adding a complex surface optical potential. The calculations in Fig. 11 were generated by using a halo type density distribution for ^{6}He. Both ^{6}He density distributions have the same root mean square matter radius of 2.54 fm. The predicted cross sections for angles larger than 23 degrees (see Fig. 10 and Fig. 11) are different depending on the ^{6}He density. Indeed, some sensitivity to the shape of the density distribution can be obtained from precise large angle elastic scattering measurements.

The ensemble of these experimental studies [27], [37] indicates that to describe elastic scattering of weakly bound nuclei, a polarization potential has to be added to the bare potential.
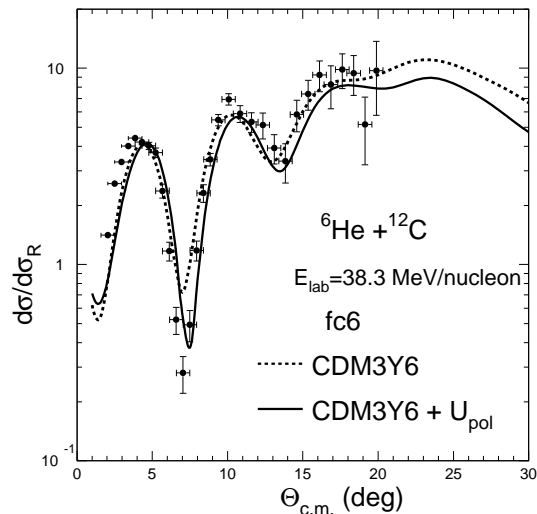
Fig. 11. The same as Fig. 10 but the optical model calculations were obtained with folding model optical potentials generated with a halo type shape density distributions for ^{6}He.

3   Inelastic scattering and magic numbers

3.1   Highlights

Magic numbers have been for years one of the milestones in nuclear physics. However, they should not be considered as fixed properties all along the nuclear chart, but rather as local properties depending on N and Z, the numbers of neutrons and protons. The usual level ordering is shown in Fig.12, with the single particle energies versus the quadrupolar deformation and the successive major shell gaps for N = 8, 20, 28 in stable nuclei. Deviations from that picture were found as soon as very neutron rich nuclei became available, the sodium isotopes and their descendants produced at CERN. Many anomalies were observed, at variance with the trend expected for N = 20 nuclei, one of them being the quite low energy, E_{2+} = 880 keV, of the first 2^+ excited state in ^{32}Mg [38]. Finally, the open question is: how do the magic numbers (and shell effects) evolve from stability to the drip-lines, with possible vanishing of old or appearance of new magic numbers? The structure properties may be investigated with global observables, like the existence, the mass, the period or the level scheme in β decay. However, β decay requires large beam intensities and does not necessarily populate all the accessible levels in the daughter nuclei, with possible uncertainties in the spin assignment.

Direct reactions are necessary to go further and inelastic scattering will provide information on collective observables.
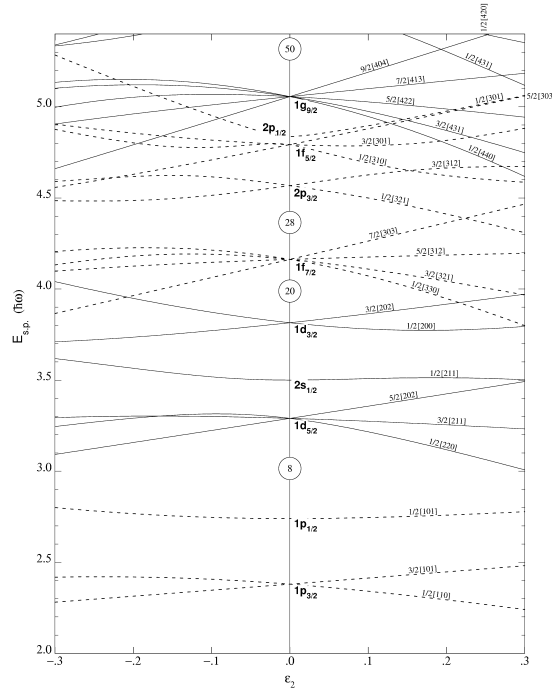

Fig. 12. Single particle energies versus the quadrupolar deformation

Coulomb excitation has been recently reinvestigated with exotic projectiles on heavy targets like ^{197}Au and ^{208}Pb at high incident energy. In this case, the interaction time is very short and only the lowest-lying states in the projectile can be excited. The Coulomb interaction favours low angular momentum transfer and is very well suited for the study of the first 2^+ excited state in even nuclei. There are two parameters to be measured, the excitation energy and the inelastic scattering cross section $\sigma_{exc}(0^+ \rightarrow 2^+)$ from which we may deduce the B(E2,$0^+ \rightarrow 2^+$). The B(E2,$0^+ \rightarrow 2^+$) is relevant to the collectivity of the nucleus and can be compared to microscopic model predictions. In the standard rotational model, it is connected to the static deformation β_2 and radius R_c of

the charge density by the relation

$$B(E2, 0^+ \rightarrow 2_1^+) = (\frac{3Ze}{4\pi})^2 (\beta_2)^2 R_c^4$$

For closed shell nuclei, the large gap to the next available shell is responsible for the rather high energy of the 2^+ excited state. The spherical shape corresponds to low B(E2) values. This behavior is clearly seen for the closed shell N = 20 nuclei ^{40}Ca and ^{36}S in Fig.13. For an increasing neutron number, the energy decreases and the B(E2) increases [39], which is indicative of some collectivity. This trend goes on even for ^{44}S and N = 28 [40], at variance with ^{48}Ca.

In the case of ^{32}Mg at N = 20, the B(E2) was found to be large, a value which is not compatible with a spherical nucleus [41]. In this mass region, there is a competition in the ground state wave function between the normal shell model configuration $(d3/2)^4$ and the intruder one $(d3/2)^2(fp)^2$. The latter is favoured in case of a quadrupolar (prolate) deformation.
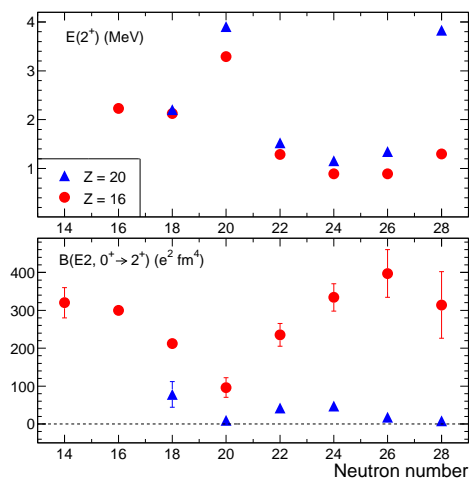

Fig. 13. (top) Energy of the first 2^+ excited state; (bottom) B(E2,$0^+ \rightarrow 2^+$) of the even sulphur and calcium isotopes versus the neutron number N.

Another example may be found at the shell closure N = 8 far from stability for Be isotopes. In that case, there is a competition between the 1p1/2 sub-shell and the intruder 2s1/2 sub-shell which is expected to be over the major shell gap in the usual shell model. One explanation may be a gap reduction due to the spin-orbit interaction for a large neutron excess.

^{11}Be is a famous illustration, with its unexpected $1/2^+$ ground state and $1/2^-$ first excited state. The energy of the transition $1/2^- \rightarrow 1/2^+$ is small, E_γ = 320 keV, with a strong E1 strength, B(E1) = 0.1 $e^2 fm^2$ which is expected in the case of quasi-degenerate subshells [42–44].
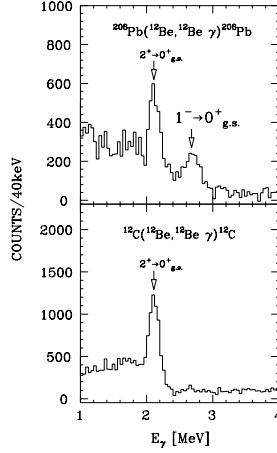
Fig. 14. Doppler-corrected γ-ray energy spectra measured in the inelastic scattering of ^{12}Be on lead (top) and carbon (bottom) targets

Coulomb excitation and (p,p') inelastic scattering were recently used [45,46] to study the level scheme of ^{12}Be. A level was observed at 2.68 MeV (Fig.14) in the inelastic scattering of ^{12}Be + ^{208}Pb [45], at variance with the same reaction with a ^{12}C target, dominated by the nuclear interaction. For that reason, an E1 transition was assumed and a 1^- assignment proposed for this low-lying state, with a large E1 strength, B(E1) = 0.051 e^2fm^2. Inelastic scattering of ^{10}Be and ^{12}Be on a proton target were compared [46] to infer collectivity in ^{12}Be, although the B(E2) value for ^{12}Be remains unknown. The structure of ^{12}Be was also investigated with the one neutron knock-out reaction at MSU [47]. The ground state was found to be a mixture of the two components $(\nu 1p1/2)^2$ and $(\nu 1p1/2)^0(\nu 2s1/2)^2$ with equal weights. All these data seem consistent with a reduction of the shell closure N = 8 near the neutron drip-line.

The next Be isotope, ^{13}Be, is unbound. The structure of its ground state is still an open question both from an experimental [48,49] and theoretical point of view. The relative ordering of the 1p1/2, 2s1/2 and 2d5/2 sub-shells in ^{13}Be as well as the B(E2) value for ^{12}Be are of crucial importance for the description of the halo nucleus ^{14}Be. We would not like to close this point without stressing the importance of the l = 0 sub-shell 2s1/2 and its radial extent in the description of halo nuclei like ^{11}Li, ^{11}Be or ^{14}Be.

Otsuka et al. [50] propose a generalized description of these shell evolutions in terms of the spin-isospin interaction $V_{\sigma\tau}$. It is the attractive interaction of valence protons with $j_> = l + 1/2$ and neutrons with $j_< = l - 1/2$ (or the opposite) which is responsible for a binding gain of the neutron $j = l - 1/2$ sub-shell. The weakening of that attraction for $\pi d5/2$ protons and $\nu d3/2$ neutrons (resp. $\pi p3/2$ protons and $\nu p1/2$ neutrons) when less protons occupy the valence

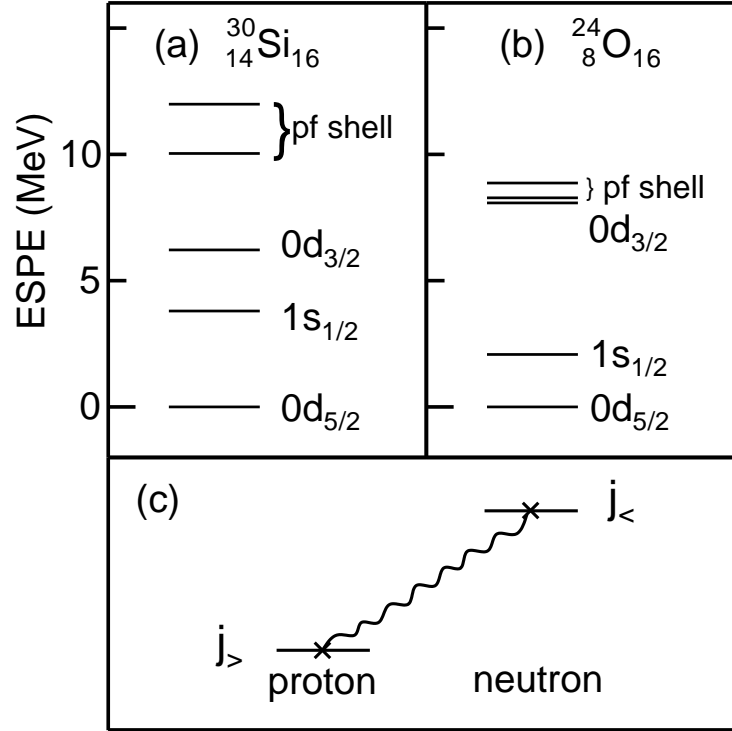proton sub-shell may explain the vanishing of N = 20 (resp. N = 8), see also Fig.15.

Fig. 15. Scheme of the attractive interaction $V_{\sigma\tau}$ and its influence [50] on the two N = 16 nuclei ^{30}Si and ^{24}O, with a closed and empty proton $d5/2$ sub-shell, respectively.

So far, we have described the evolution of shell closures established for stable nuclei with a general trend for a disappearance or at least a weakening when the neutron excess is increased. There is a case for which the opposite trend was recently proposed [51] and a new magic number N = 16 might appear. This is connected to the level density in the sd shell. For neutron rich nuclei and low binding energy, a gap may appear between the 2s1/2 and 1d3/2 sub-shells. This effect is again explained in the case of a weaker occupancy of the proton $\pi d5/2$ valence sub-shell [50]. Then, the $\nu d3/2$ neutron sub-shell is less bound and may even be degenerate with the fp sub-shells. The maximum effect is expected with ^{24}O for an empty $\pi d5/2$ sub-shell, Fig. 16. First indications may be seen 1) in the mass surfaces showing discontinuities for shell closures, 2) in a significant increase from the expected trend of interaction cross sections measured [51] on a carbon target for N = 15 and Z < 10. Moreover, the neutron drip line is

observed at N = 16 from Z = 6 to 8, since all the oxygen isotopes from ^{25}O to ^{28}O are unbound [52], fixing the Z = 8 neutron drip-line at ^{24}O. With S_{2n} = 6.45 MeV for ^{24}O, this suggests a very strong binding-loss, adding neutrons towards ^{26}O and ^{28}O. If the $\nu d3/2$ and νfp neutron sub-shells are degenerate, ^{28}O is not doubly magic, which could explain the lack of extra binding and its non-existence. Note that with only one proton more, the fluorine isotopes are bound at least up to ^{31}F [52]. However, these experimental indications are far from conclusive and additional proofs have to be given, like the measurement of the first 2^{+} excited state in ^{24}O or microscopic information provided by transfer reactions.
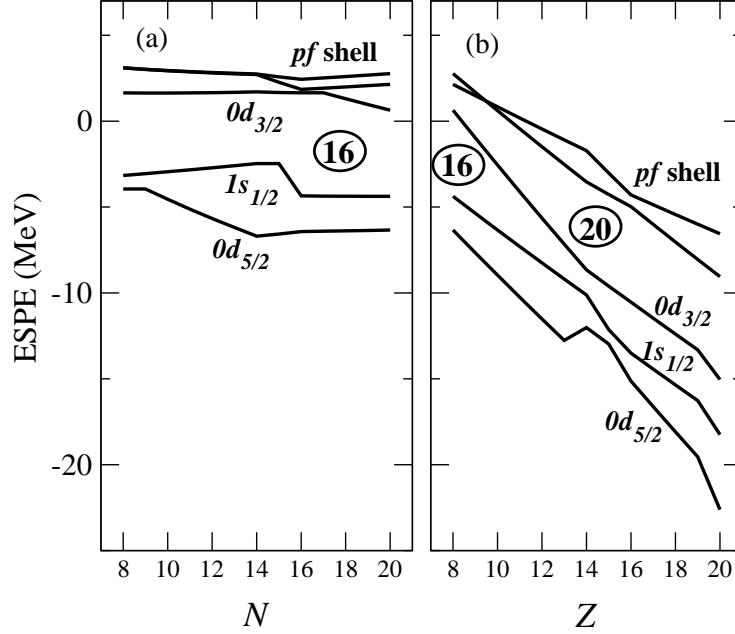

Fig. 16. (left) Evolution of the sd + fp subshells for the oxygen isotopes with a nearly constant gap for N = 16; (right) the same for the N = 20 isotones.

3.2   Selected examples of proton inelastic scattering

Proton inelastic scattering has provided a wealth of information on nuclear structure and interaction potentials. With the advent of radioactive beams, proton inelastic scattering is used as a complementary probe to Coulomb excitation measurements. Electron scattering probes mainly the protons in the nucleus while proton scattering probes both protons and neutrons. In this chapter we will present results and theoretical analyses of proton inelastic scattering on S isotopes and ^{6}He.

An exciting aspect of radioactive beam studies is the search for the onset of major structural changes, such as the weakening of major shell closures far from stability. The region of the N=28 shell closure has also proven to be of particular interest and experimental and theoretical work has been dedicated to determining the properties of the first 2^+ excited states of S isotopes. Coulomb excitation studies performed on neutron-rich even-even sulphur ^{38,40,42,44}S isotopes yielded energies and reduced transition probabilities $B(E2)$ that showed a weakening of the N=28 shell closure far from stability. Subsequently, proton scattering experiments were performed for ^{38,40}S and more recently for ^{30,32}S. While the Coulomb force is known exactly, the analysis of proton scattering data must rely on nuclear models, the parameters of which need to be adjusted to reproduce experimental results. We will discuss both phenomenological and microscopic models used to analyse selected proton inelastic scattering data on S isotopes and we will show that the nuclear structure information obtained from these analyses is less "model dependent" than is commonly believed.

3.3   Proton inelastic scattering on S isotopes

Two interesting quantities which reveal the relative contribution of protons and neutrons to the excitation of a nucleus are the multipole transition matrix elements M_p and M_n given by the relation:

$$M_{n,(p)}^{\lambda} = \int \rho_{tr,\lambda}^{n(p)} r^{\lambda+2} dr$$

The proton transition matrix element M_p, in the case of a transition from a 0^+ state to an excited 2^+ state, is related to the reduced transition probability $B(E2)$ by $B(E2)=M_p^2$. In the standard collective model, where deformation lengths for protons and neutrons are equal, $M_n/M_p=N/Z$.

The M_n/M_p ratio may be determined by comparing the excitation by different external probes which have different interaction strengths for protons and neutrons, such as Coulomb excitation and proton scattering. In phenomenological analyses, M_n/M_p is obtained by using an empirical formula established by Bernstein et al., [53] for $\lambda = 2^+$ and 3^- transitions:

$$\frac{M_n}{M_p} = \frac{b_p^p}{b_p^n}\{\frac{\delta_N}{\delta_{em}}(1 + \frac{b_n^p N}{b_p^p Z}) - 1\},$$

where b_p^p and b_p^n are the proton-proton and proton-neutron interaction strengths and δ the usual deformation parameters for nuclear excitation δ_N and electromagnetic excitation δ_{em}. To extract the nuclear deformation length, the angular distributions of scattered protons are generally analysed using distorted wave Born approximation (DWBA) or coupled channels calculations with a phenomenological form factor which assumes either vibrational or rotational behaviour. The optical potentials needed to generate the entrance and exit channel distorted waves are usually taken from the global analysis of Bechetti and

Greenlees [2] and are of Woods-Saxon type. The extracted M_n/M_p ratios for $^{30-40}$S are presented in table 1. The M_n/M_p ratio for ^{38}S is of the order of 1.5, indicating a significant isovector contribution to the 2^+ state. We would like to remind the reader that in a simple collective model the oscillation of the homogeneous neutron-proton fluid is so-called purely isoscalar if $M_n/M_p = N/Z$. Consequently, a significant deviation of M_n/M_p from N/Z indicates the degree of what we call the isovector mixing in the quadrupole excitations considered. For this reason, there is a well-established tradition of presenting the ratio M_n/M_p divided by N/Z, as in Table 1. However, it is well known that this phenomenological approach suffers from ambiguities and must be calibrated for each multipolarity using known transitions in nearby nuclei. The validity of this prescription is even more uncertain in the case of unstable nuclei where often the neutron and proton density and concomitantly the corresponding potentials have different root-mean-square radii.

We will present JLM and folding model microscopic calculations for describing inelastic scattering of S isotopes. The aim of these calculations is to demonstrate that the ratio M_n/M_p can be obtained in a rather model independent way.

α) JLM model microscopic calculations

In the first calculation the original JLM model with shell model ground state and transition form factors is used to generate inelastic scattering angular distributions. The results of these calculations are denoted as JLM_{SM} [13]. In the second example the original JLM model is used with ground state and transition densities generated from self-consistent quasi-particle quantum random phase approximation calculations ($QRPA$). The results of these calculations are denoted as JLM_{QRPA} [12]. The third results denoted as JLM_{HFB}^{M} [11] corresponds to calculations obtained by using the modified JLM-Bruyères code with ground state and transition densities obtained from constrained Hartree-Fock-Bogoliubov (HFB) calculations based on the finite range, density dependent D1S force. Finally, we present calculations based on a new M3Y folding formalism with ground state and transition densities provided by HF plus BCS and QRPA approaches respectively. The results of these calculations are denoted as $M3Y_{QRPA}$ [16].

Calculations with shell model densities

JLM_{SM}: From the valence shell model point of view, the proton and neutron multipole matrix elements M_p, M_n are constructed from the valence matrix elements A_p, A_n by:

$$M_p = (1 + C_{pp})A_p + C_{pn}A_n$$

$$M_n = (1 + C_{nn})A_n + C_{np}A_p$$

where C_{cv} are the generalized effective charges due to polarization of the core (c) nucleons by the valence (ν) nucleons. For the sd shell nuclei when both protons and neutrons are in the same valence shell it is a good approximation to assume that $C_{pp} = C_{nn}$ and $C_{pn} = C_{np}$. For these nuclei the experimental data are consistent with an average value of the generalized effective charges of 0.35, although some fluctuations do exist [54].

In Fig. 17 the shell model transition density for the excitation of the 2^+ state of ^{32}S is compared with the experimental results obtained from inelastic electron scattering measurements. The good agreement between the shell model calculations and the experimental results gives us confidence in the ability of the shell model approach to compute realistic density distributions.
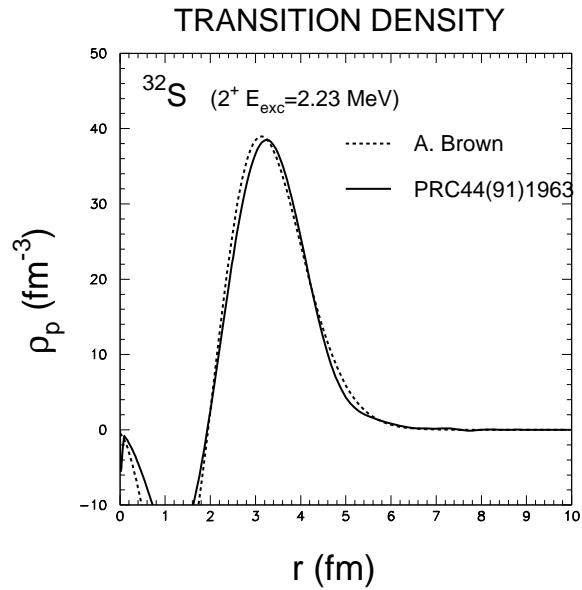

Fig. 17. Transition-density distributions for the first 2^+ state of ^{32}S. The full curve corresponds to the experimental results obtained by inelastic electron scattering and the dotted curve to the shell model calculations.

The analysis within the JLM_{SM} folding model of the elastic and inelastic scattering data provided an M_n/M_p ratio of the order of 1.0, which is the expected value in the limit where the neutron and proton deformations are the same and N=Z, as is the case for ^{32}S.

In Fig. 18 the angular distributions for the 2^+ states in the ^{32,38,40}S(p,p') reactions are presented together with JLM folding model calculations with neutron and proton transition densities obtained from shell model calculations. For

all the calculations the same renormalization of the entrance channel optical potential was assumed in both elastic and inelastic scattering calculations, $\lambda_v=1.0$ and $\lambda_w=0.8$. For ^{32}S the solid line presents a calculation with $B(E2)=300e^2fm^4$ and $M_p = M_n$. A good agreement with the data is observed without any new adjustment of the entrance channel potential. The experimental $B(E2)_{exp}$ value is (300 ± 13) e^2fm^4. An equally good agreement with the data is obtained by using the experimental transition density distributions presented in Fig. 17. In a pioneer work on JLM calculations [55], we have analysed $0^+ \Rightarrow 2^+$ inelastic scattering data for nuclei like ^{18}O, ^{30}Si, ^{32,34}S, ^{48}Ca and ^{88}Sr for which the proton and neutron transition densities and therefore the values of the M_p and M_n transition matrix elements are known from electron and high energy proton inelastic scattering measurements. For the same nuclei we have analysed low energy inelastic scattering angular distributions in the JLM_{SM} formalism and M_p and M_n transition matrix elements were also obtained. We have shown that these indirectly extracted values agree rather well with the experimentally obtained M_p and M_n. In this paper we have shown for the first time in an unquestionable way that the JLM approach is well suited for obtaining structure information in the case of stable nuclei.
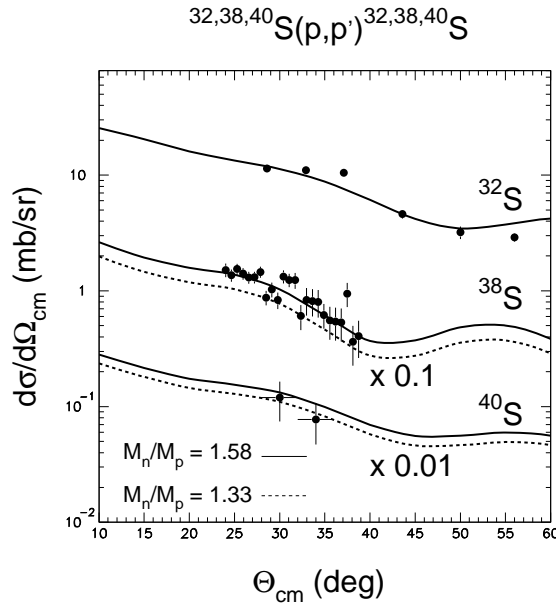

Fig. 18. Angular distributions for the 2^+ state in the ^{32}S(p,p') at 53 MeV/nucleon, the ^{38}S(p,p') at 39 MeV/nucleon and ^{40}S(p,p') at 30 MeV/nucleon, together with JLM_{SM} calculations, see text.

For nuclei such as ^{38}S where the protons and neutrons are in different valence orbits, the generalized effective charges may be different. Indeed, to reproduce the $B(E2)=M_p^2=245.3e^2fm^4$ value for ^{38}S obtained by the electromagnetic excitation measurements of Glasmacher et al., [40] it was necessary to modify the effective charges. A good agreement with the data was obtained by assuming $C_{pp} = C_{nn} = 0.35$ and $C_{pn} = C_{np} = 0.65$. For ^{38}S C_{pn} is larger than C_{pp} because in these shell model calculations the neutron valence space was truncated to include only the $p_{3/2}$ and $f_{7/2}$ shell so that the effective charge has to account for the $p_{3/2}-f_{5/2}$, $p_{3/2}-p_{1/2}$ and $f_{7/2}-f_{5/2}$ transitions, and because the overall effective charge in the fp shell may be larger, due to the larger size of the valence fp orbits relative to the size of the sd orbits. With these new values of the generalized effective charges and with $A_p = 5.42$ and $A_n = 12.84$, obtained by using harmonic oscillator wave functions, we obtain from the previous equation $M_n/M_p = 1.33$.

With no-core $6\hbar\omega$ calculations for ^{6}Li, Navrátil et al. [56] have shown that model-space truncation is sufficient to generate operator renormalization, which is characterized by effective charges compatible with those used in phenomelogical applications. The isoscalar and isovector parts of the operators are normalized differently leading to a nonzero neutron effective charge. This is the microscopic origin of effective charges in the shell model, but such a discussion goes beyond the scope of the present paper.

In the case of the ^{38}S exotic nuclei, experimental transition densities do not exist and therefore for analysing the data we rely on theoretical transition density distributions. In this way, we test simultaneously the models from which the densities were obtained. In this respect for ^{38}S neutron and proton densities for the entrance channel potential and transition form factors were provided by shell model calculations, with $M_n/M_p = 1.33$. The calculated ^{38}S(p,p') inelastic scattering angular distribution, given by the dotted line in Fig. 18, rather underestimates the data, indicating that the assumed M_n/M_p ratio is not adequate for ^{38}S. However, since the value of M_p was obtained from electromagnetic excitation measurements, the only unknown quantity for analysing the inelastic scattering results is the M_n value, or the ratio M_n/M_p. In order to fit the data, the ratio of the multipole matrix elements had to be changed to $M_n/M_p = 1.58$, the solid line in Fig. 18, which corresponds to an effective neutron charge of C_{nn}=0.65. This increase of the value of C_{nn} from 0.35 to 0.65 may be related to the truncation in the orbitals used for neutrons. With this new value for the effective charge we obtain a reasonable agreement with the experimental results. Similar conclusions can be drawn for ^{40}S. The dotted line corresponds to a calculation with $C_{pp} = C_{nn} = 0.35$ and $C_{pn} = C_{np} = 0.65$, the solid line to a calculation with C_{nn}=0.65. The situation in the ^{40}S 2^+ inelastic scattering is uncertain because the comparison is based on two data points only, with large experimental uncertainties. One clearly needs more experimental information in order to draw reliable conclusions.

The multipole matrix elements $(M_n/M_p)/(N/Z)$ for S isotopes, obtained within the different theoretical approaches are presented in Table 1.

Calculations with QRPA densities

JLM_{QRPA}: The microscopic analysis of the data was performed using a QRPA model and the JLM interaction [12]. E. Khan and his collaborators [12] have developed a self-consistent QRPA model built on top of a HF+BCS mean field. The QRPA calculations overestimate the excitation energies of the first 2^+ states of the S isotopes by around 700 keV, but the evolution along the isotopic chain is rather well reproduced. The calculated $B(E2)$ values are acceptable within the experimental error bars, except for ^{36}S for which the theoretical $B(E2)=241e^2fm^4$ is very large, $(B(E2)_{exp}=(96\pm26)\ e^2fm^4)$. This nucleus is known to present a puzzle because several microscopic models are unable to reproduce its properties. Inelastic scattering calculations were performed for the S isotopes. The theoretical proton transition density was renormalized to reproduce the $B(E2)$ values measured by electromagnetic probes. This renormalization is small, at least for the S isotopes, since the calculated $B(E2)$ values are in good agreement with the data, with the exception of ^{36}S. Once the M_p value is fixed the M_n value is deduced by renormalizing the neutron transition density in order to reproduce the measured (p,p') inelastic scattering angular distributions. Optical potential normalization factors $\lambda_v=1.0$ and $\lambda_w=0.8$ were also used in these calculations. The calculations give a rather good account of the (p,p') data. The extracted multipole matrix elements $(M_n/M_p)/(N/Z)$ are presented in Table 1. Apart from the nucleus ^{36}S no compelling experimental evidence for isovector excitations is found, in agreement with the QRPA theoretical predictions, but at variance with the phenomenological predictions which indicate a strong isovector contribution to the 2^+ state of ^{38}S and probably of ^{40}S, see below. The multipole matrix elements obtained presently are in very good agreement with the results obtained by the JLM_{SM} using shell model transition matrix elements.

Calculations with HFB densities

JLM^M_{HFB}: In this study the spherical optical model was extended to treat proton scattering by deformed nuclei [11]. Briefly, a collective Hamiltonian expressed in terms of the five quadrupole collective degrees of freedom is built from constrained Hartree-Fock-Bogoliubov calculations based on the finite range, density dependent D1S force. Radial densities for protons and neutrons in a nucleus are deduced from the calculated matrix elements and used within the JLM approach. Once the ground state and the transition potentials are obtained, they are inserted into the ECIS98 code [57] to solve the coupled channels equations for elastic and inelastic scattering. In these calculations no effective charges or free parameters are introduced with the exception of a small readjustment of the λ_v and λ_w values which is not significant considering the experimental error.

Except for ^{36}S and an underestimation of the cross section of the 2^+ state in the case of ^{38}S, the microscopic calculations are in agreement with the experimental results. The multipole matrix elements $(M_n/M_p)/(N/Z)$ from these
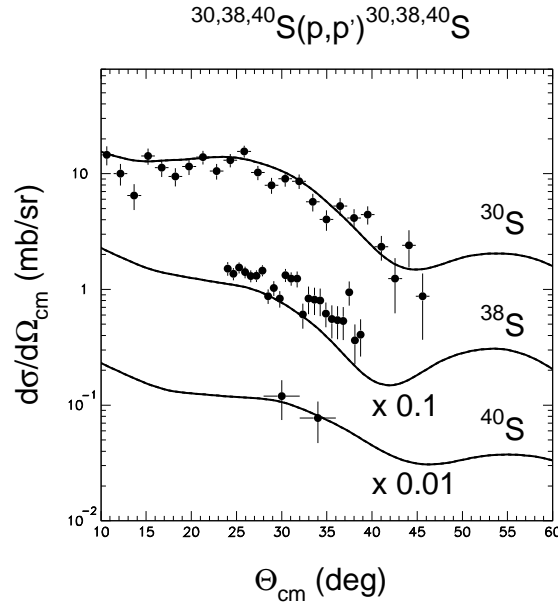
Fig. 19. Microscopic coupled channel calculations using microscopic collective model densities and the Bruyères-JLM nucleon-nucleon interaction for the ground state (Fig.5) and the 2^+ state in the ^{30}S(p,p') at 53 MeV/nucleon, the ^{38}S(p,p') at 39 MeV/nucleon and ^{40}S(p,p') at 30 MeV/nucleon.

microscopic collective model calculations are also presented in Table 1. In the case of ^{36}S, a renormalization of the transition densities entering into the JLM calculations by a factor of 0.5 produces theoretical calculations which are in good agreement with the data. This further confirms that the microscopic collective model overestimates by a factor of 2 the deformation of the single closed shell nucleus ^{36}S. Indeed, this approach adopts the picture of large amplitude collective motion which is not the appropriate picture for a closed-shell nucleus. However, as was previously discussed, the QRPA method, which relies upon the assumption that collective modes are of small amplitude character, is also unable to reproduce the properties of ^{36}S. This situation is really puzzling and we believe that not only additional theoretical but also experimental investigations concerning this nucleus are called for.

β) folding model microscopic calculations

The folding formalism for the nucleus-nucleus potential [58] was adapted recently to a single folding formalism for elastic and inelastic nucleon-nucleus potentials using the density- and isospin dependent M3Y (CDM3Y6) interac-

tion. Detailed folding analyses of proton elastic and inelastic scattering were performed within this formalism [16]. The contribution from the isoscalar and isovector parts of the proton-nucleus optical potential and inelastic form factors were treated explicitly in each case to study the isovector mixing effect in proton-nucleus scattering as one goes along the isotopic chain from proton rich ^{30}S to the neutron rich $^{38,40}S$ isotopes. However, since the original M3Y interaction is real, the folding formalism generates the real parts of the elastic and inelastic nucleon-nucleus potential only. The imaginary potential is obtained from the CH89 global systematic and is readjusted to fit the experimental angular distributions [16].

The analysis of the inelastic scattering results was performed within the standard DWBA approach using QRPA transition densities. The results for ^{38}S+p elastic and inelastic scattering are compared with the data in Fig. 20. The inelastic form factors were obtained from renormalized QRPA transition densities, as was done for the JLM_{QRPA} calculations. The deduced multipole matrix elements for the S isotopes are presented in Table 1. The results obtained for $^{36,38}S$+p are puzzling. They are different to the values obtained by the JLM approaches using different microscopic transition densities. The comparison is particularly significant in the case of the JLM_{QRPA} calculations, where the same structure input but two different reaction models were used. This casts some doubt on the multipole matrix elements obtained experimentally through these approaches, or at least adds an error bar to the multipole matrix elements due to the scattering model used, and calls for a deeper theoretical understanding of the reaction models involved in these analyses.

Table 1. Multipole matrix elements $(M_n/M_p)/(N/Z)$ for S isotopes. The $(M_n/M_p)/(N/Z)$ value for ^{34}S indicated in the JLM_{SM} calculation is obtained from [55]. In the case of the JLM_{HFB}^M results the quoted $(M_n/M_p)/(N/Z)$ ratios correspond to theoretical predictions. In this model also the theoretical results underestimate the ^{36}S experimental angular distributions. A renormalization of the transition densities by a factor of 0.5 produces predictions in good agreement with the data.

Nucleus	E_2^+	Phenom	JLM_{SM}	JLM_{QRPA}	JLM_{HFB}^M	$M3Y_{QRPA}$
^{30}S	2.24	0.93±0.20		0.88±0.21		1.05
^{32}S	2.21	0.95±0.11	1.0±0.20	0.94±0.16	0.965	0.96
^{34}S	2.12	0.91±0.21	0.95±0.10	0.85±0.23	0.921	1.04
^{36}S	3.29	1.13±0.27		0.65±0.18	1.043	0.90
^{38}S	1.29	1.50±0.30	1.16±0.15	1.09±0.18	1.085	1.44
^{40}S	0.89	1.25±0.25	0.93±0.20	1.01±0.27	1.120	1.17

It is interesting to compare the results of these different microscopic analyses. We have used different structure inputs, namely Shell model, $(QRPA)$ and
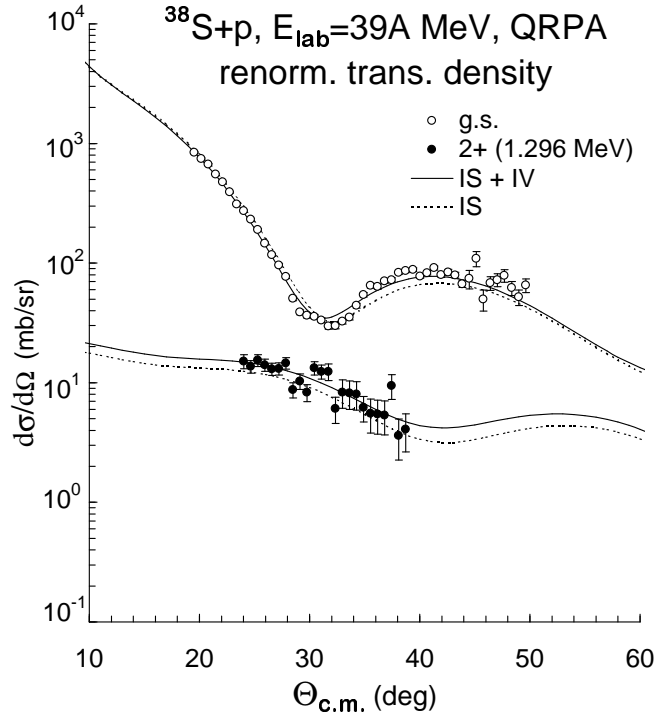
Fig. 20. Elastic and inelastic ^{38}S+p scattering data compared to the DWBA cross sections given by the elastic and inelastic potentials folded with the HF+BCS ground-state and renormalized QRPA transition densities, respectively. The cross sections given by the isoscalar potentials alone are plotted as dotted curves.

Hartree-Fock-Bogoliubov (HFB) calculations to generate ground state and transition densities. The JLM approach was used in all these calculations to generate entrance channel optical potentials and inelastic scattering transition potentials. The DWBA TAMURA [59] code was used to calculate elastic and inelastic angular distributions in the case of the Shell model and ($QRPA$) approach. The ECIS [57] coupled channels code was used in the case of the Hartre-Fock-Bogoliubov approach. The multipole matrix elements obtained from these analyses are in very good agreement with each other, indicating the robustness of the general approach. A major goal of the present studies is to find observables sensitive to the presence of neutron skins. The deduced (M_n/M_p) ratios for all isotopes, except ^{36}S, are close to (N/Z). The HFB results suggest a slight increase of the $(M_n/M_p)/(N/Z)$ ratio towards the neutron rich isotopes, which is not present for the QRPA calculations. Moreover, these approaches are very efficient in testing microscopic nuclear densities and concomitantly the ability of microscopic models to reproduce proton and neutron transition matrix elements. It is interesting to observe that the HFB calculations which constitute today probably the most sophisticated microscopic approach are not able to reproduce the p+^{38}S inelas-

tic scattering results. The availability of a new generation of radioactive beam facilities will allow us to extend these studies to more neutron rich nuclei and obtain additional information on the strength of the N=28 shell closure far from stability. Concerning the presently studied S isotopes, neither the experimental results nor the theories indicate a clear isovector behaviour except for ^{36}S, contrary to that suggested by the phenomenological and folding model microscopic analysis.

Proton inelastic scattering on ^{6}He

The structure of ^{6}He was explored with proton elastic and inelastic scattering to the first 2^+ excited state (Q=-1.8 MeV) of ^{6}He in inverse kinematics using a ^{6}He beam of 41.6 MeV/nucleon at GANIL [60] and of 24.5 MeV/nucleon in DUBNA [61].

Both experimental results were analysed by the theoretical formalism developed by K. Amos et al., [18]. Calculations of the transition amplitudes for the inelastic scattering have been done within the distorted wave approximation (DWA). For the stable nuclei whose spectroscopy is defined from measurements of inelastic electron scattering form factors, the inelastic scattering has been shown to be very sensitive to the details of the effective interaction. Conversely, when the effective interaction is well established, the analysis of inelastic scattering data turns out to be a very sensitive test of the model structure used for the nucleus. With the effective NN interaction set, it remains only to define the structure of ^{6}He. The Navrátil and Barrett [62] large space shell model calculations were used in the scattering analyses of both experiments [60], [61]. Their complete $6\hbar\omega$ wave functions were used to specify the relevant ground state and $0^+ \rightarrow 2^+$ one body-density matrix elements for ^{6}He. However, to investigate the sensitivity of the analyses to the size of the model space, wave functions from a complete $4\hbar\omega$ shell model calculation [19] were also used. In both cases the binding energy of the last neutron is larger than the experimental separation energy of 1.87 MeV, indicating that the size of the model space is still too small to give the correct asymptotic behaviour of the neutron density.

In Fig. 21 we present calculations performed within the JLM model and the present sophisticated approach. Wave functions from the same complete $4\hbar\omega$ shell model were used in both calculations. The theoretical predictions agree with each other, but don't reproduce the experimental angular distributions. The calculations made with the shell model using HO wave functions are indicated as *no halo*. To obtain a *halo-like* description of ^{6}He, the HO wave functions were replaced by WS wave functions which furthermore were adjusted so that binding energies of the higher orbits were all set to 0.5 MeV. In that sense the labelling of *halo* and *no halo* is used merely to distinguish between the two sets of calculations. The *no halo* and *halo-like* density distributions have root mean square radii of 2.3 and 2.58 fm, respectively.

The elastic scattering data are compared in Fig. 22(a) to the halo (solid line) and no halo (dashed line) calculations. The two calculations are very similar up
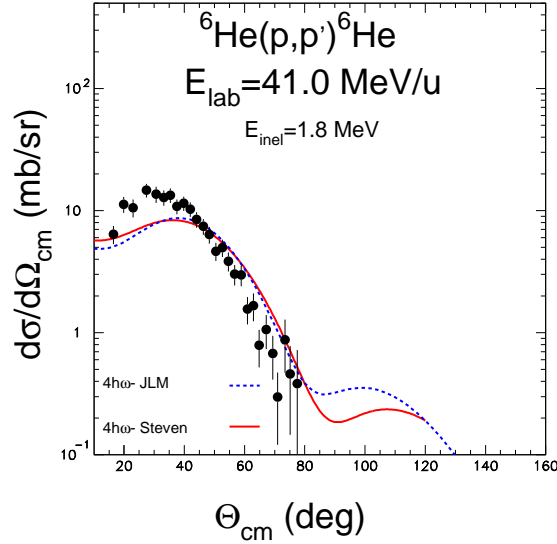
Fig. 21. Theoretical calculations performed within the JLM approach $(4h\omega JLM)$ and within the present sophisticated approach by Steven Karataclidis $(4h\omega - Steven)$. Transition densities and wave functions from the same shell model calculation are used as input in both calculations

to $60°$ and notably different at larger angles. The agreement of the calculations with the data is very good up to $60°$. The few data points beyond these angles are better reproduced by the halo description but it is clear that data at larger angles are required to use elastic scattering as a probe of the halo structure of ^{6}He. The very good agreement obtained with the elastic scattering data is essential since it validates the folding optical potential used to define the distorted waves in the DWA analysis of the inelastic scattering leading to the 2^+; $T = 1$ state. Halo (solid line) and no halo (dashed line) calculated cross sections for the 2^+ state are presented in Fig. 22(b). Contrary to the elastic scattering, the sensitivity to the halo is important over the entire angular domain. The data are better reproduced by the halo calculation.

Similar conclusions are obtained by the 24.5 MeV/nucleon [61] experiment. In Fig. 23 the 24.5 MeV/nucleon and the 40.9 MeV/nucleon elastic (top) and inelastic (bottom) data are shown as a function of the momentum transfer. The 24.5 MeV/nucleon data are denoted by solid circles and the 40.9 MeV/nucleon data by open circles. The solid and dashed curves are the *halo-like* model prescriptions.

For both experiments the 2^+ state scattering data are not reproduced by using the unaltered shell model wave functions which over-predict the binding
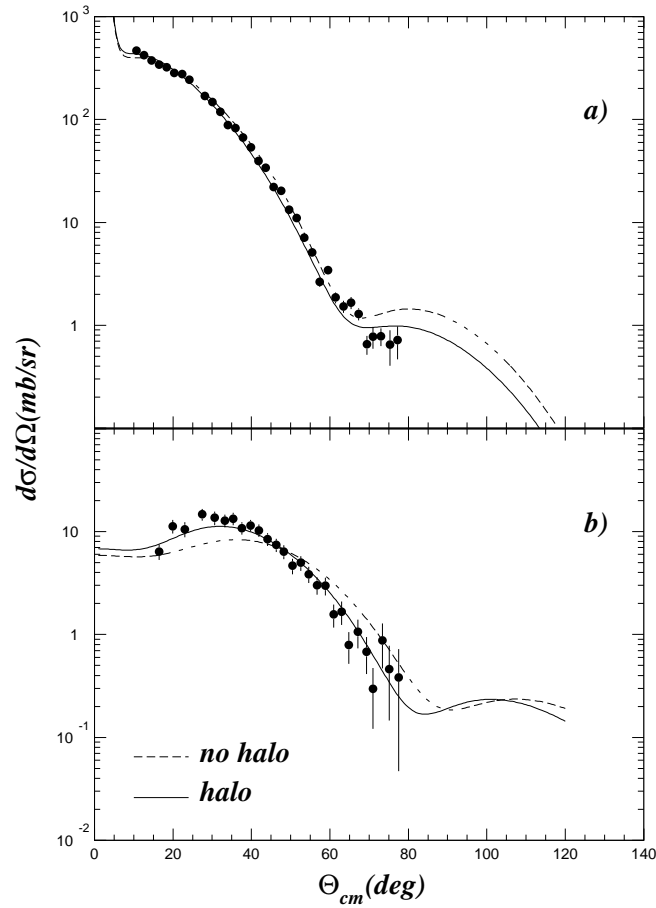
Fig. 22. Differential cross sections for the (a) elastic and (b)inelastic scattering to the of 2^+ state at 1.87 MeV of ^{6}He from hydrogen at $40.9A$ MeV. The present data (circles) are compared to the results of the calculations assuming no halo (dashed line) and halo (solid line) conditions.

energy of the valence neutrons and thus do not allow the halo to be formed. The sensitivity of the inelastic scattering data to the structure of ^{6}He opens large perspectives for the study of the microscopic structure of exotic systems.
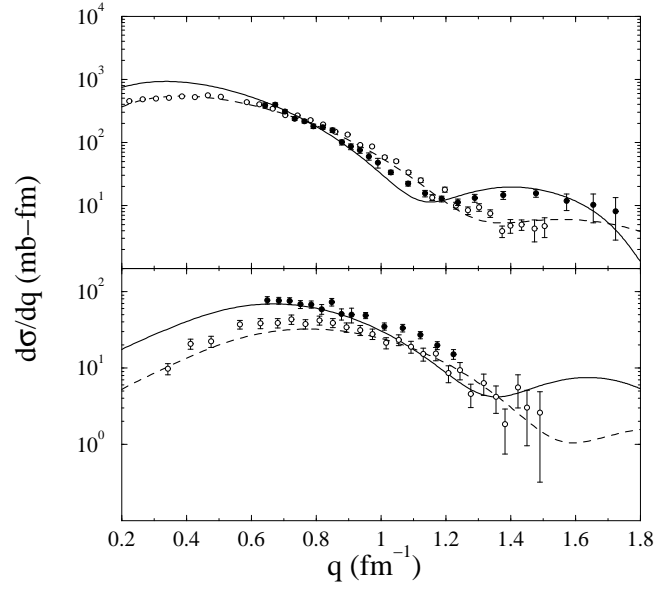
Fig. 23. Differential cross sections for the elastic (top) and inelastic (bottom) scattering to the 2^+ state of ^{6}He as momentum transfer functions. The data taken with $24.5A$ MeV (solid circles) and $40.9A$ MeV (open circles) beams are compared to calculations assuming halo conditions.

4   Transfer reactions

Very few transfer reaction studies involving radioactive beams have been carried out so far. This is mainly due to the low cross section, of the order of 1 mb/sr. For low beam intensities it is necessary to use thick targets, which is contradictory to good resolution in excitation energy. This point may be overcome if high resolution γ-ray detectors are used in coincidence to improve the excitation energy resolution. However, a new limitation appears due to the limited γ-ray detection efficiency which implies a 4π γ-ray geometry. Moreover, the requirement of γ-ray detection limits the method to the study of bound states.

As previously mentioned, the ground state of ^{11}Be has an unexpected $J^\pi = 1/2^+$ instead of $1/2^-$ structure. The simplest configuration consists of a $2s1/2$ valence neutron coupled to a ^{10}Be core, that is $|^{10}\text{Be}(0^+) \otimes 2s1/2 >$. In case of core excitation (2^+ excited state at 3.368 MeV for ^{10}Be), there is another component with a valence neutron in the $1d5/2$ sub-shell, that is $|^{10}\text{Be}(2^+) \otimes 1d5/2 >$. If one expresses the wave function of the $1/2^+$ ^{11}Be ground state as the sum of the single-particle and core excited components

$$^{11}Be_{gs} = \alpha |^{10}Be(0^+) \otimes 2s1/2 > +\beta |^{10}Be(2^+) \otimes 1d5/2 > \tag{1}$$

the spectroscopic factors for transfer to the ground and first excited state of ^{10}Be should by directly related to α^2 and β^2 respectively. There are large differences in the ratio β/α between the present theoretical calculations, from nearly 0 in [63] to 0.73 in [64].

The study of the neutron transfer ^{11}Be (p,d) ^{10}Be provides information on the overlap between the ground state in ^{11}Be and the 0^+_{gs} and 2^+_1 states in ^{10}Be as well as on the ratio of the two components β/α. The experiment was done in inverse kinematics. The ^{11}Be beam bombarded a CH_2 target. The ejectiles were detected within the SPEG spectrometer and the CHARISSA detector array[65]. In Fig.24, the transfer to the 0^+_{gs} and 2^+_1 at 3.4 MeV in ^{10}Be is clearly identified, once the deuterons are selected in CHARISSA.

The analysis of such data is far from simple for many reasons. The first one is the imperfect knowledge of the potential in the entrance and exit channels, especially for nuclei very far from stability for which coupling effects to the continuum are important. In the standard DWBA calculations with single-particle form factors (the usual separation energy prescription), the spectroscopic factors $S(0^+)$ and $S(2^+)$ deduced from the experiment have large error bars. The 2^+ admixture in the wave function of ^{11}Be is given by the ratio $R_{ce} = \frac{S(2^+)}{S(0^+)+S(2^+)}$, for which a lower limit of 30% is obtained. However, the separation energy prescription may fail in that case, due to the collectivity of ^{10}Be, with a large value for B(E2) = 52 e^2fm^4. A substantial correction may be expected due to coupling to the excited core. In that case, the spectroscopic factor $S(2^+)$ is significantly reduced and consequently the ratio R_{ce} is about 20%.
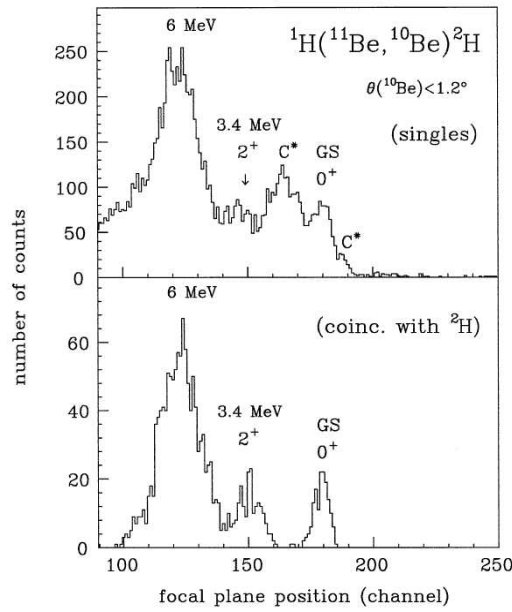
Fig. 24. Focal plane spectra of ^{10}Be from the ^{1}H(^{11}Be,^{10}Be)^{2}H transfer for singles (top) and ^{10}Be in coincidence with deuterons in CHARISSA (bottom)

These results are in agreement with another experimental approach, the one neutron knock-out reaction. In this case, a ^{11}Be projectile at 60 A.MeV interacts in the field of a ^{9}Be target, and the ^{10}Be ejectile is analyzed and identified by the S800 spectrometer at MSU [66]. From the parallel momentum distribution of ^{10}Be (Fig. 25), the dominance of the $\ell = 0$ component in the wave function of ^{11}Be is clearly established.
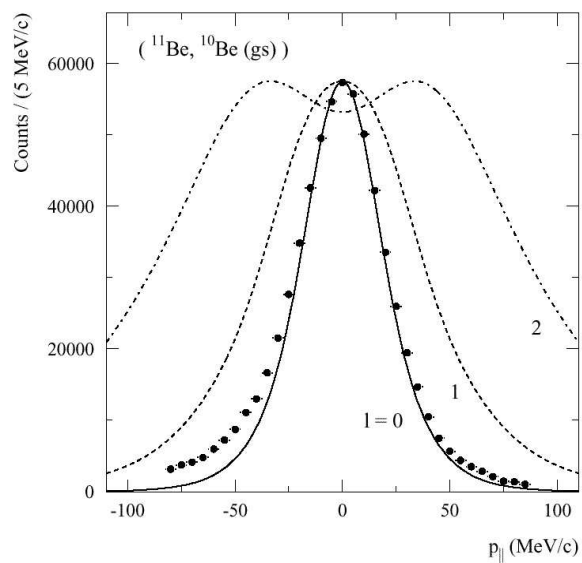
Fig. 25. Parallel momentum distribution of the ^{10}Be fragments after selection of the ground state [66]. The three curves correspond to a calculation in an eikonal model for the knockout process. The best agreement is obtained for the full line and $\ell = 0$.

5   Sub-barrier fusion

With the advent of radioactive beam facilities, interest in near and sub-barrier fusion studies with halo nuclei was renewed due to their specific features, like extended neutron densities, low-lying continuum, and very low energy thresholds for breakup. Indeed, fusion, as other reaction processes, (elastic scattering,...) is expected to be affected by such features.

From the theoretical point of view, it is expected that fusion cross sections for halo nuclei will present an increase due to the decrease of the potential barrier and the coupling to soft vibrational modes [67]. This increase, however, according to several elaborate but contradictory theories, may be hindered or enhanced due to break-up processes [68–73].

The first measurements with halo nuclei were performed for the systems ^{11}Be+^{209}Bi [74], ^{6}He+^{209}Bi [75] and ^{6}He+^{238}U [76]. The data are presented in Fig. 26 together with the data of the associated stable isotopes ^{9}Be+^{209}Bi [74], ^{4}He+^{209}Bi [77] and ^{4}He+^{238}U [76,78].

For ^{9,11}Be+^{209}Bi and ^{4,6}He+^{209}Bi the detection of the fusion products was carried out via their characteristic delayed α-particle activities. This technique leads to a rather precise measurement of the fusion cross section. In contrast, for ^{4,6}He+^{238}U what was measured is the fission cross section. Fission can also be triggered by inelastic or transfer reaction events. In such cases the fission would be accompanied by a residue of the projectile. Although it was verified that contributions corresponding to multiplicity equal to three were very small [76], in a recent and more elaborate experiment it was shown that the two data points well below the Coulomb barrier are essentially due to a transfer like process, see below. In any case, it may be and it was correctly assumed that around the Coulomb barrier the fission cross section is very close to the fusion cross section.

Special attention has to be paid when comparing the systems ^{6}He+^{209}Bi and ^{4}He+^{209}Bi. The compound nucleus ^{215}At formed via the ^{6}He+^{209}Bi fusion reaction decays exclusively by evaporation of 2, 3 or 4 neutrons. The total fusion cross section for the system ^{6}He+^{209}Bi was obtained by adding the 3n and 4n channels. Indeed, the effect of the 2n channel is small except at energies well below the barrier [75]. In this respect, it is compared to the ^{4}He+^{209}Bi fusion cross section obtained by adding only the 2n, 3n and 4n channels, which makes this comparison meaningful. As will be shown later on, to obtain the total fusion cross section for the system ^{4}He+^{209}Bi, one has to add the 1n channel. Cross sections are presented in Fig. 26 as a function of energy divided by the Coulomb barrier, V_b. For details see [79].

The presentation of all the data in Fig.26 leads to the following conclusions. For energies higher than the Coulomb barrier the cross sections for the fusion of ^{4,6}He+^{238}U and ^{4,6}He+^{209}Bi present the same behaviour. No enhancement is observed for the fusion of ^{6}He over that of ^{4}He above the barrier. For energies lower than the Coulomb barrier, the fusion cross section for the halo nucleus ^{6}He is enhanced over that of ^{4}He at least for ^{209}Bi. On the other hand, for energies higher than the Coulomb barrier the fusion cross section of ^{11}Be+^{209}Bi
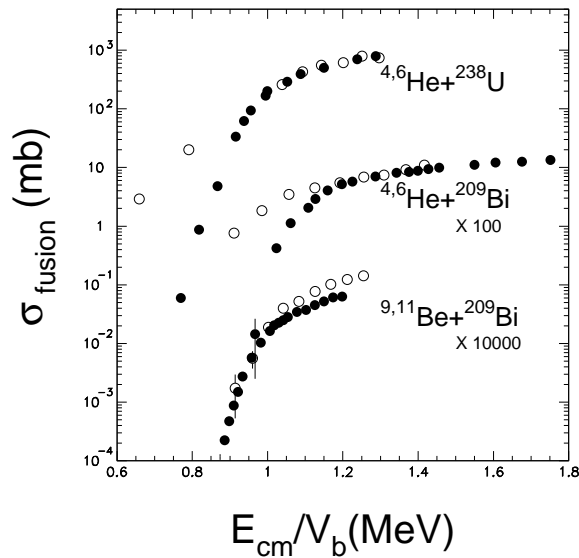
Fig. 26. Comparison of fusion cross section measurements for halo (open circles) and their associate stable systems (closed circles). The data are from references [74–78]

is enhanced over that of ^{9}Be+^{209}Bi, while, no such enhancement is observed below the barrier.

Most of the results concerning the fusion of two nuclei under and near the Coulomb barrier were interpreted adequately well within the framework of coupled channels (CC) calculations [80]. This kind of calculation with phenomenological nucleus-nucleus potentials can successfully reproduce a vast amount of data [81]. The main ingredients of such calculations, performed here with the ECIS code [57], are the entrance channel potential and the structure of the colliding nuclei. The structure of the colliding nuclei is taken explicitly into account via folding models. The entrance channel potential can be traditionally inferred by elastic scattering data at energies well above the Coulomb barrier. The overall success of realistic folding models for the description of elastic scattering data of stable nuclei, without any renormalization N_R of the real potential (N_R close to unity) indicates that the real dynamic polarization potential (DPP) is weak, except for the scattering of weakly bound nuclei due to breakup effects, as discussed in chapter 2.3.

Coupled channels calculations were performed for the data presented in Fig. 26 [79]. The real part of the entrance potential was calculated within the double folding model by using the BDM3Y1 interaction. As was mentioned, this interaction was found to describe rather well elastic scattering data for both
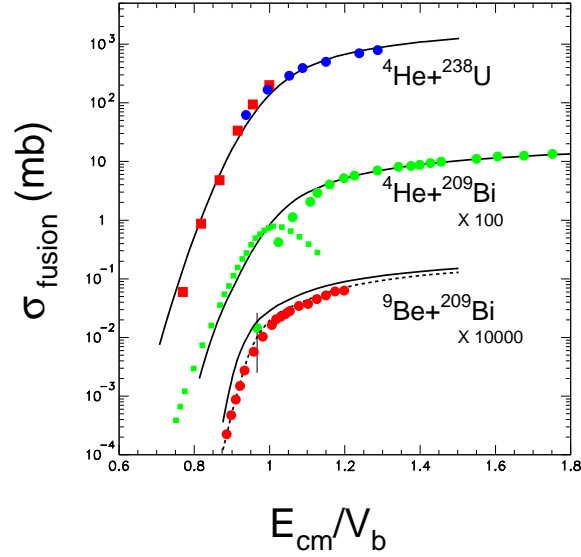
Fig. 27. Fusion cross section measurements for stable nuclei are compared with CC calculations with a non-reduced optical potential. The data for the system ^{4}He + ^{238}U with circles come from reference [76] while with squares from reference [78]. The data for the system ^{4}He+^{209}Bi with circles come from reference [77] and refer to a sum of the 2n, 3n, 4n evaporation channels while the squares come from ref [82] and refer to the 1n evaporation channel.

stable and weakly bound nuclei [28,26] as long as the normalization factor is substantially reduced for the weakly bound nuclei. The normalization factor of the entrance channel potential was set equal to unity (N_R=1) for the stable isotopes (^{4}He+^{238}U and ^{4}He+^{209}Bi) and equal to N_R=0.6, 40% or to N_R=0.4, 60% for the stable weakly bound and unstable nuclei.

The calculations for the systems ^{4}He+^{238}U, ^{4}He+^{209}Bi and ^{9}Be+^{209}Bi are compared with the experimental data in Fig. 27. We point out that the additional data indicated in Fig. 27 with squares, correspond to the 1n evaporation channel of the reaction ^{209}Bi(α,n)^{212}At [82]. The experimental results can be reproduced equally well within this model without any reduction of the potential for the ^{4}He projectiles. Concerning the system ^{9}Be+^{209}Bi, calculations have been performed for a non-reduced potential (solid line) and for a reduced potential (dashed line). As can be seen, the adopted 40% reduction of the potential according to the elastic scattering data is adequate to describe the sub-barrier and near barrier fusion data.

The calculations performed for the halo projectile systems are compared with the experimental data in Fig. 28. Good agreement with the data for ^{6}He+^{238}U

and ^{6}He$+^{209}$Bi is obtained with a 60% reduction of the potential at and above the Coulomb barrier. This reduction is compatible with the calculations of R. Raabe [83] within the continuum discretized coupled channels framework. Below the Coulomb barrier the calculations fail to reproduce the data for ^{6}He$+^{238}$U but, in a new and more precise experiment, it was shown that the two data points below the barrier are essentially due to transfer-like reactions [83].
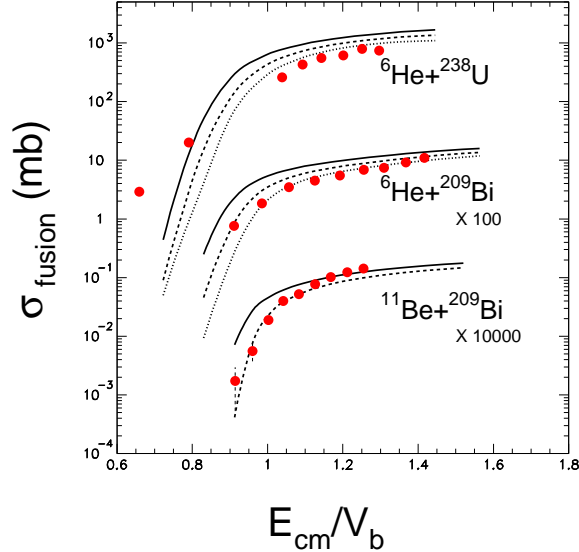

Fig. 28. Fusion cross section measurements for halo systems are compared with CC calculations with a non-reduced (N_R=1) optical potential -solid line - and a reduced N_R=0.6 optical potential -dashed line. The dotted line for the system ^{6}He$+^{238}$U and ^{6}He$+^{209}$Bi corresponds to a calculation with a reduction of the optical potential of N_R=0.4

Below the Coulomb barrier the reduction for ^{11}Be$+^{209}$Bi is of the order of 40%. However, for energies well above the Coulomb barrier the ^{11}Be$+^{209}$Bi system is better described with non-reduced potential calculations.

From this analysis we can draw the conclusion that the CC calculations, taking into account in a simplistic way the break-up effects via a reduced potential, reproduce the gross properties of near and sub-barrier fusion, including weakly bound nuclei. The agreement of the calculations with the data is particularly spectacular in the case of the system ^{9}Be$+^{209}$Bi where the exact reduction of the potential was known from elastic scattering data at energies well above the Coulomb barrier. For the unstable systems the situation seems to be more com-

plicated, probably due to the lack of elastic scattering results at energies around and well above the Coulomb barrier.

Concerning sub-barrier fusion, coupled channels calculations were performed for several systems with haloes and their associated non-halo projectiles. From the analysis of these pioneer experiments it was found that a fundamental difference occurs between stable and unstable systems. The dominant channel in the barrier energy region of stable systems is fusion. For unstable and weakly bound nuclei this is not the case. Loss of flux through other channels like breakup takes place, and can be taken into account by the reduction of the entrance channel optical potential, i.e. exactly in the same way as for elastic scattering data. In that respect, the description of the weakly bound systems -(^{9}Be+^{209}Bi), (^{9}Be+^{208}Pb) and the halo systems- ^{6}He+^{209}Bi, ^{6}He+^{238}U and ^{11}Be+^{209}Bi - was obtained by making use of a reduced potential to account for the breakup processes. For the halo systems only a qualitative agreement was obtained.

More elaborate theoretical approaches (continuum discretized coupled channels calculations) and additional measurements, including elastic scattering, complete fusion (without contributions due to incomplete fusion) and breakup are necessary in order to obtain a more comprehensive picture of near- and sub-barrier fusion involving halo nuclei.

References

1. J.J. Kelly *et al.*, Phys. Rev. **C47** (1993) 2146, and references therein.
2. F.D. Bechetti and G.W. Greenlees Phys. Rev. **182** (1969) 1190.
3. J.P. Jeukenne, A. Lejeune, C. Mahaux, Phys. Rev. **C16** (1977) 80, and references therein.
4. N. Alamanos and P. Roussel-Chomaz, Ann. Phys. **Fr.21** (1996) 601, and references therein.
5. S. Mellena *et al.*, Phys. Rev. **C28** (1983) 2267.
6. J.S. Petler *et al.*, Phys. Rev. **C32** (1985) 673.
7. V. Lapoux *et al.*, Phys. Lett. **B517** (2001) 18.
8. V. Lapoux et al., to be published in Yadernaya Fizika "Physics of Atomic Nuclei" the Proceedings of the VIIth Int School-Seminar on Heavy Ion Physics (HIPH'02) 20-25th June 2002.
9. R. De Leo *et al.*, Nuovo Cimento **A59** (1980) 101.
10. J.H. Kelly *et al.*, Phys. Rev. **C56** (1997) R1206.
11. F. Maréchal *et al.*, Phys. Rev. **C60** (1999) 034615.
12. E. Khan et al., Nucl. Phys. **A694** (2001) 103.
13. N. Alamanos, F. Auger, B.A. Brown and A. Pakou, J. Phys. **G24** (1998) 1541.
14. G.R. Satchler and W.G. Love, Phys. Reports **55** (1979) 183.
15. E. Bauge, J.P. Delaroche and M. Girod, Phys. Rev. **C58** (1998) 1118.
16. D. T. Khoa et al., Nucl. Phys. **A706** (2002) 61.
17. D. T. Khoa, W. von Oertzen and H. G. Bohlen, Phys. Rev. **C49** (1994) 1652, Phys. Lett. **B342** (1995) 6.
18. K. Amos, P.J. Dortmans, H.V. von Geramb, S. Karataglidis and J. Raynal, Adv. Nucl. Phys. **25** (2001) 275.
19. S. Karataglidis *et al.*, Phys. Rev. **C61** (2000) 024319.
20. K. Amos, S. Karataglidis and P.K. Deb, Phys. Rev. **C65** (2002) 064618.
21. C. Jouanne et al., Preprint DAPNIA-02-118 (2002).
22. S. Fortier et al., Phys. Lett. **B461**(1999)22.
23. Y. Blumenfeld et al., Nucl. Instr. and Meth. in Phys. Res. **A421**(1999) 471.
24. S. Ottini-Hustache et al., Nucl. Instr. and Meth. in Phys. Res.**A431** (1999) 476.
25. M. El-Azab Farid and G.R. Satchler, Nucl. Phys. **A441** (1985) 157 and **A438** (1985) 525.
26. Dao T. Khoa, G.R. Satchler and W. von Oertzen, Phys. Rev. **C56** (1997) 954.
27. Dao T. Khoa, G.R. Satchler and W. von Oertzen, Phys. Rev. **C51** (1995) 2069.
28. L. Trache *et al.*, Phys. Rev. **C61** (2000) 024612.
29. D. T. Khoa, W. von Oertzen *et al.*, Phys. Lett. **B342** (1995) 6.
30. A. Pakou *et al.*, Phys. Lett. **B556** (2003) 21.
31. G. R. Satchler *et al.*, Ann. Phys. **178** (1987) 110.
32. Y. Sakuragi, Phys. Rev. **C35** (1987) 2161.
33. W.G. Love, T. Terasawa and G.R. Satchler, Phys. Rev. Lett. **39** (1977) 6.
34. R. Donangelo, L.F. Canto and M.S. Hussein, Nucl. Phys. **A320** (1979) 422.
35. G. Pollarolo, R.A. Broglia and A. Winther, Nucl. Phys. **A406** (1983) 369.
36. Z. El-Itaoui, P.J. Ellis and B.A. Mughrabi, Nucl. Phys. **A441** (1985) 511.
37. V. Lapoux *et al.*, Phys. Rev. **C66** (2002) 034608.
38. C. Detraz et al., Nucl. Phys. **A394** (1983) 378 and D. Guillemaud et al., Nucl. Phys. **A426** (1984) 37.
39. H. Scheit et al., Phys. Rev. Lett. **77** (1996) 3967.
40. T. Glasmacher et al., Phys. Lett. **B395** (1997) 163.

41. T. Motobayashi et al., Phys. Lett. **B346** (1995) 9 and B.V. Pritychenko et al., Phys. Lett. **B461**(1999) 322 and V. Chiste et al., Phys. Lett. **B514**(2001) 233.
42. D.J. Millener et al., Phys. Rev. **C28** (1983) 497.
43. T. Nakamura et al., Phys. Lett. **B394** (1997) 11.
44. M. Fauerbach et al., Phys. Rev. **C56** (1997) R1.
45. H. Iwasaki et al., Phys. Lett. **B491** (2000) 8.
46. H. Iwasaki et al., Phys. Lett. **B481** (2000) 7.
47. A. Navin et al., Phys. Rev. Lett. **85** (2000) 266.
48. A.V. Belozyorov et al., Nucl. Phys. **A636** (1998) 419.
49. M. Thoennessen et al., Phys. Rev. **C63**(2001) 014308.
50. T. Otsuka et al., Eur. Phys. J. **A15** (2002) 151.
51. I. Tanihata, Nucl. Phys. **A682**(2001) 114C.
52. H. Sakurai, Phys. Lett. **B448** (1999) 180.
53. A.M. Bernstein, V.R. Brown and V.A. Madsen, Comment Nucl. Part. Phys. 11 203.
54. B.A. Brown *et al.*, Phys. Rep. **5** (1983) 313.
55. N. Alamanos, A. Pakou, A. Lagoyannis and A. Musumarra, Nucl. Phys. **A660** (1999) 406.
56. P. Navrátil, M. Thoresen and P.R. Barett, Phys. Rev. **C55** (1997) R573.
57. J. Raynal, Phys. Rev. **C23** (1981) 2571.
58. D.T. Khoa and G.R. Satchler, Nucl. Phys. **A668** (2000) 3.
59. T. Tamura *et al.*, Comp. Phys. Commun. **2** (1971) 94.
60. A. Lagoyannis *et al.*, Phys. Lett. **B518**(2001) 27.
61. S.V. Stepantsov *et al.*, Phys. Lett. **B542**(2002) 35.
62. P. Navrátil and B. R. Barrett, Phys. Rev. **C54** (1996) 2986; *ibid* **C57** (1998) 3119.
63. P. Descouvemont, Nucl. Phys. **A615**(1997) 261.
64. T. Otsuka et al., Phys. Rev. Lett. **70** (1993) 1385.
65. S. Fortier et al., Phys. Lett. **B461** (1999) 22 and J.S. Winfield et al., Nucl. Phys. **A683**, 48 (2001)
66. T. Aumann et al., Phys. Rev. Lett. **84**, 35 (2000)
67. N.Takigawa and H. Sagawa, Phys. Lett. **B265** (1991) 23.
68. M. S. Hussein and M. P. Pato, Phys. Rev. **C46** (1992) 377.
69. C. H. Dasso and A. Vitturi, Phys. Rev. **C50** (1994) R12.
70. N. Takigawa, M. Kuratani and H. Sagawa, Phys. Rev. **C47** (1993) R2470.
71. M. S. Hussein *et al.*, Phys. Rev. **C46** (1992) 377.
72. M. S. Hussein and A. F. de Toledo Piza, Phys. Rev. Lett. **72** (1994) 2693, Phys. Rev **C51** (1995) 846.
73. K. Hagino *et al.*, Phys. Rev. **C61** (2000) 037602.
74. C. Signorini *et al.*, Eur. Phys. J. **A227** (1998) 157.
75. J. J. Kolata *et al.*, Phys. Rev. **C81** (1998) 4580.
76. M. Trotta *et al.*, Phys. Rev. Lett. **84** (2000) 2342.
77. W. J. Ramler *et al.*, Phys. Rev. **114** (1959) 154.
78. V. E. Viola and T. Sikkeland, Phys. Rev. **128** (1962) 767.
79. N. Alamanos *et al.*, Phys. Rev. **C65** (2002) 054606.
80. S. G. Steadman and M. J. Rhoades-Brown, Ann. Rev. Part. Sc. **36** (1986) 649.
81. G. Pollarolo and A. Winther, Phys. Rev. **C62** (2001) 054611-1.
82. A. R. Barnett and J. L. Lilley, Phys. Rev. **C9** (1974) 2010.
83. R. Raabe et al. private communication and to be published.